Accepted Manuscript

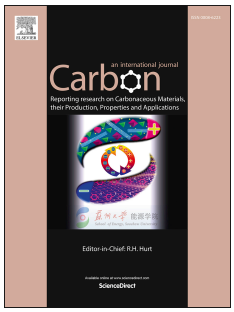

High-power nitrided TiO_2 carbon felt as the negative electrode for all-vanadium redox flow batteries

J. Vázquez-Galván, C. Flox, J.R. Jervis, A.B. Jorge, P.R. Shearing, J.R. Morante

PII: S0008-6223(19)30075-2

DOI: https://doi.org/10.1016/j.carbon.2019.01.067

Reference: CARBON 13871

To appear in: *Carbon*

Received Date: 1 November 2018

Revised Date: 7 January 2019

Accepted Date: 19 January 2019

Please cite this article as: J. Vázquez-Galván, C. Flox, J.R. Jervis, A.B. Jorge, P.R. Shearing, J.R. Morante, High-power nitrided TiO_2 carbon felt as the negative electrode for all-vanadium redox flow batteries, *Carbon* (2019), doi: https://doi.org/10.1016/j.carbon.2019.01.067.

GRAPHICAL ABSTRACT

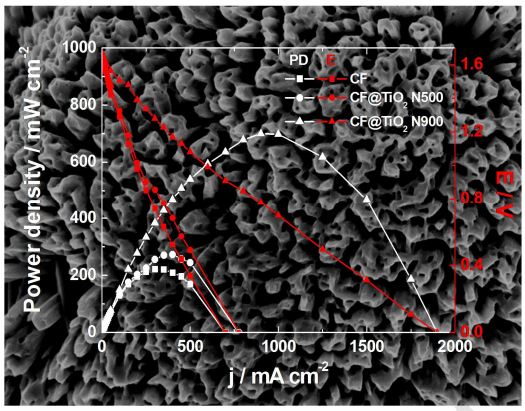

High-power nitrided TiO_2 carbon felt as the negative electrode for all-vanadium redox flow batteries

*J. Vázquez-Galván**[a], *C. Flox**[a], *J. R. Jervis*[c] *A. B. Jorge*[d], *P.R. Shearing*[c] *and J. R. Morante*[a,b]

[a] Catalonia Institute for Energy Research (IREC), Jardins de les Dones de Negre, 1, 08930 Sant Adrià del Besos (Spain).

[b] Departament d'Electronica, Universitat de Barcelona C. de Martí I Franquès, 1, 08028 Barcelona (Spain).

[c] Department of Chemical Engineering, University College London, Torrington Place, London, WC1E 7JE, United Kingdom

[d] Materials Research Institute, School of Engineering and Materials Science, Queen Mary University of London, Mile End Rd, London, E1 4NS, United Kingdom

KEYWORDS: Energy Storage• Titanium nitride •VRFB •High-power density• Nitrided TiO_2 decorated carbon electrodes• negative electrodes for VRFB.

ABSTRACT. This work describes the design of an electrode with enhanced performance applied to all-vanadium redox flow batteries (VRFBs). This new electrode consists of a structural porous carbon felt decorated with TiO_2 rutile nanoparticles, which has been nitrided using ammonolysis at 900 ºC. An outstanding charge and mass transfer over the electrode-electrolyte interface was observed as a consequence of the synergetic effect of N- and O-functionalization over carbon felt (CF) and the partial formation of TiN (metallic conductor) phase. Moreover, this material has not only improved in terms of catalysis towards the V^{3+}/V^{2+} redox reaction (k_0= 1.6 x 10^{-3} cm s^{-1}), but also inhibited the hydrogen evolution reaction (HER), which is one of the main causes of imbalances that lead to battery failure. This led to an impressive high-power peak output value up to 700 $mW\ cm^{-2}$, as well as work at high current density in galvanostatic conditions (i.e. 150 $mA\ cm^{-2}$), exhibiting low ohmic losses (overpotential) and great redox single cell reversibility, with a superior energy efficiency of 71%. An inexpensive, earth abundant and scalable synthesis method to boost VRFBs technology based on nitrided CF@TiO_2 is presented, being able to overcome certain constrains, and therefore to achieve high energy and power densities.

1. INTRODUCTION

Stationary energy storage systems have increased in relevance over the past decade because of their important role in grid-scale applications, contributing to systems such as intermittent renewable power sources, smart-grid integration and energy self-consumption to guarantee the electrical supply in remote areas. In this framework, the important role of vanadium redox flow batteries (VRFBs) towards providing clean and affordable energy has been well-reported in the literature.[1–4] Nevertheless, the practical implementation of this mature technology has been hampered due to their high capital cost, proving to be a critical factor for the widespread commercialization. Recently, viability studies showed that the cost of VRFB for frequency regulation is about \$560 / *kWh*,[5] making VRFBs economically uncompetitive systems.[6,7]

The cost and performance of the stack is influenced by three components: 1) membrane[8–10]; 2) electrodes[11–18] and 3) bipolar plates[19–21]. Special attention should be paid to the electrodes since they support the electrode kinetics and determine the overpotential and, consequently, the efficiency of the entire system. In addition to this, the 3D porous structure of the electrodes determines the flow and permeability characteristics that influence the mass transport overpotential incurred during operation, as well as the pressure drop across the electrode[22]. It is well known that improvements in the electrochemical performance of the electrodes can be achieved by either increasing their surface area or their electrochemical activity. At this point, it should be considered that the reported values for the kinetic constant associated to V^{3+}/V^{2+} redox reaction, k_0, spread over three orders of magnitude, showing that the surface characteristics have a strong influence on the electrochemically active surface area, as well as the reaction rate

constant. Consequently, the study of the influence of functional groups over the surface properties and k_0 values is still a fundamental open question[23]. Contrary to the initial expectations considering the simplicity of the reaction mechanisms[24], kinetics towards V^{2+}/V^{3+} are far less favoured comparatively to the VO^{2+}/VO_2^{+} redox reaction[25], limiting the cell performance. This is a particular problem due to the sluggish kinetics of the V^{2+}/V^{3+} redox couple at the negative electrode occurring at -0.26 V *vs.* SHE (1), more negative than the hydrogen evolution reaction (HER) (2) in highly acidic electrolyte[26–29].

$$\mathbf{V^{3+} + e^- \leftrightarrow V^{2+}} \qquad \mathbf{E^0 = -0.26\ V\ vs.\ SHE} \qquad \mathbf{(1)}$$

$$\mathbf{2H^+ + 2\,e^- \leftrightarrow H_2} \qquad \mathbf{E^0 = 0\ V\ vs.\ SHE} \qquad \mathbf{(2)}$$

Furthermore, this fact coupled with a high charge transfer resistance (R_{ct}) of the carbon felt electrode leads to a large overpotential of the system, preventing the charge process achieving 100% state-of-charge (SoC) and lowering voltage and energy efficiency of the battery. We have previously demonstrated[29] improved performance by the implementation of hydrogen-treated TiO_2 electrodes, which enhances the electrode's electrical conductivity, leading to a small overpotential and low charge transfer resistance.

In this context, recent research [30,31] have focused on the potential enhancement of performance due to the presence of oxygen and nitrogen-based functional groups at the surface of the electrodes, as a consequence of an increase of the electrochemical kinetics of the V^{2+}/V^{3+} redox reaction. Wei *et. al*. demonstrated that TiN bonds at the electrode/electrolyte interface are able to react with vanadium to form the stable V-N-Ti intermediate, necessary for the electron transfer process[30]. Additionally, TiN has also

received substantial attention, owing to its large electrical conductivity (10^{-4} *S* cm^{-1})[32] and high stability in strong acid media[33], which in our case, coupled with the functionalization of the carbon structure, contributes to the enhancement of the electrocatalytic activity towards the V^{2+}/V^{3+} redox reaction. By growing TiO_2 nanowires onto the surface of the graphite felt via a seed-assisted hydrothermal approach, that are then nitrided to TiN, we have obtain energy efficiency values above 70% at high current densities up to 150 *mA* cm^{-2}, which evidences good stability and high capacity retention. **Figure 1** shows a comparative of the energy efficiency values from **Table S1**.

In parallel, other authors have reported on the significant role played by the C-N bonds in the interaction with the vanadium species [34]. Nitrogen-doped carbon samples have been widely investigated for electrochemical applications, especially for the oxygen reduction reaction in fuel cells, and it has been concluded that it is the facilitated adsorption of oxygen what improves the electrocatalytic activity of these carbon materials[35–38]. Moreover, it is known that after the mild oxidation of the carbon felt at 500ºC for 5 *h*. the cell energy efficiency is improved, which is attributed to the formation of oxygen related functional groups[39]. The appropriate formation of C-OH, C=O, and C-O functionalities increases the standard heterogeneous electron transfer rate for V^{3+}/V^{2+}, from 3.2x 10^{-7} to 1 x 10^{-3} *cm* s^{-1}, one of the highest values found in the literature[40]. These electrode modifications help to decrease the fraction of the current directed towards H_2 evolution in the same way as reported in our previous paper on TiO_2:H graphite felt[29]. Therefore, nitrogen modified carbon-based surfaces show a similar improvement as increasing oxygen groups on the carbon-based surfaces, making it electrochemically more active as well. Among the four main types of nitrogen groups, the quaternary or graphitic-N has been found to be the more stable in the acidic environment[39]. However, pyrrolic-N has been

proposed to be the most electrochemically active nitrogen site enhancing the catalytic activity in these nitrogen-modified carbon-based electrode materials for VRFB[41].Here, we discuss the synergetic effect of the oxygen and nitrogen groups' functionalization on the carbon-based surface, which is coupled with the nitrogen and oxygen (especially hydroxyl) group's formation from titanium-based coverage, when CF@TiO_2 is nitrided. Additionally, in the previous published paper on the role of TiN electrocatalyst in VRFB, their power-related application was not discussed and the performance evaluation being limited to the charge/discharge experiments as a proof-of-concept[30,31]. However, from the point of view of feasible applications, many efforts have been made to date to improve the peak power density as it constitutes a key parameter for the assessment of the battery power cost. For example, Aaron *et al*. demonstrated significant improvements using stacking sheets of carbon paper, achieving values up to 557 $mW\ cm^{-2}$ [1]. Liu *et al.* demonstrated a greatly improvement of this peak power values using no-gap architecture cell and thermal pre-treatment of the carbon paper electrodes, demonstrating a high-power density value of 540 $mW\ cm^{-2}$ [41]. Mayrhuber *et al.* also demonstrated an increased power density using carbon paper-based electrodes, attaining values up to 543 $mW\ cm^{-2}$ [42]. More recently, UTRC's cell technology enables substantially high power densities, where the peak power is around 1300 $mW\ cm^{-2}$ for UTRC's VRB cell [43]. In this context, due to the importance of the cell's power output, we have also analyzed the power peak density performance of the electrodes obtained applying our proposed nitride process of a carbon felt previously decorated with TiO_2. Outstanding values of power density up to 700 $mW\ cm^{-2}$ have been measured, corroborating the relevance of the proposed procedure combining the synergetic effect produced by the nitride treatment over titanium dioxide and carbon felt. This presents a procedure for increasing the current density of the system with the concomitant

decrement of the stack size cost (€ m^{-2}) and a route to lowering the large capital power-cost of VFRB ($W\ m^{-2}$).

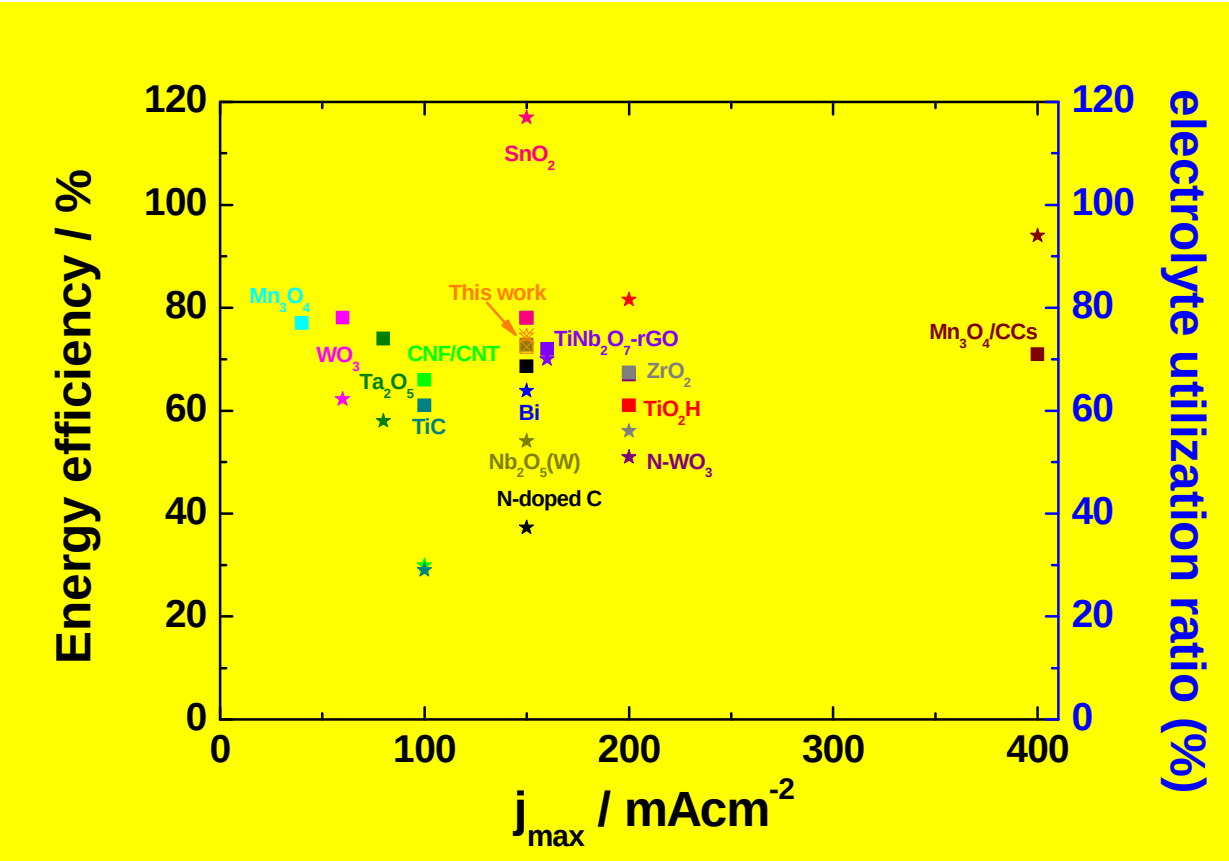

Figure 1. - Comparative of the state of the art energy efficiency and electrolyte utilization ratio related to the nitride electrode enhancement.

2. EXPERIMENTAL SECTION

2.1. Nitrided CF@TiO_2 electrode synthesis.

TiO_2 nanorods have been directly grown over a commercial carbon felt (CF, 4 cm^2 and 5 mm thickness from Mersen S.A., Spain) using a hydrothermal process reported in our previous studies[29]. Prior to this step, CF is plasma-treated in oxygen atmosphere for 10 minutes. Subsequently, an initial annealing at 500^oC for 4 *h* in O_2 atmosphere is done in order to remove all the impurities, Afterwards, TiO_2-based electrodes are nitrided by NH_3 gas at several temperatures 500 and 900^{o}C for 14 hours. The samples are labelled as CF@TiO_2N500 and CF@TiO_2N900 electrode, respectively.

2.2.CF@N900 electrode synthesis.

A commercial carbon felt (CF, 4 cm^2 and 5 mm thickness from Mersen S.A., Spain) has been modified using a hydrothermal process analogous to the nitrided CF@TiO_2 electrode synthesis but in absence on titanium precursor. Prior to this step, the CF was plasma treated in oxygen atmosphere for 10 minutes. Afterwards, the electrodes were nitrided by NH_3 gas at 900^{o}C for 14 hours in order to study the structural changes on CF. The sample is labelled as CF@N900 electrode.

2.3.CF-HT electrode synthesis.

A commercial carbon felt (CF, 4 cm^2 and 5 mm thickness from Mersen S.A., Spain) has been treated in a high vacuum plasma cleaner system (Plasma etch inc. PE-50) in oxygen atmosphere for 10 min.

2.4.Morphological and structural characterization.

The morphology and nanostructure of electrodes have been characterized with a Zeiss Serie Auriga field emission scanning electron microscope (FE-SEM). Moreover, the weight content of the different electrodes components is done by thermogravimetric analysis (TGA) in an air atmosphere. The method in all cases is an initial isothermal for 60 minutes at 30ºC, afterwards a 10ºC/min ramp up to 100ºC and holding it for 1 hour, which is followed by another 10ºC/min ramp up to 950ºC keeping that temperature for another hour and ending with a cooling down to the initial 30ºC. BET surface are for each electrode is measured in a MicroActive TriStar II 3020 using for that purpose N_2 gas. Structural characterization was carried out by X-Ray Diffraction (XRD) in a D8 Advance Bruker equipment with a Cu Kα (λ = 1.5406 Å) radiation sources working at 40 kV and 40 mA. UV/Vis absorption spectra were recorded in the diffuse reflectance mode on a PerkinElmer Lambda 950 UV/Vis spectrometer equipped with a Praying-Mantis diffuse reflectance accessory. The chemical composition changes on the surface of the electrodes were analyzed by XPS using a PHI instrument model 5773 Multi-technique with Al Kα radiation (1486.6 *eV*).

2.5.Electrochemical characterization.

A three-electrode glass cell was used to do fundamental electrochemical studies. As-prepared electrodes (0.25 cm^2) were used as working electrodes, platinum wire as counter electrode, and Hg/Hg_2SO_4 as reference electrode. Nitrogen gas was used to deoxygenate the electrolyte. Electrochemical measurements are done with a Biologic® VMP-3 multi-potentiostat controlled by EC-lab® software. The electrocatalytic reaction of the studied

electrodes towards negative reaction in VRFB was measured by cyclic voltammetry (CV) between cut-off voltages of 0.5 and -0.9 V vs. SHE at 2 mV s^{-1} scan rate in 0.05 M V^{3+} and 1 M H_2SO_4, obtaining the fundamental parameters, detail as follow: i) Current density values for oxidation and reduction peaks (I_{pa}, I_{pc}); ii) Onset potential and peak potential (E_a, E_c); iii) The ratio of oxidation and reduction peak current densities (I_{pa}/I_{pc},); and iv) and peak-to-peak potential separation. Moreover, the mass transfer negative electrode-electrolyte has been obtained from CV at different scan rates, from 2 to 50 mV s^{-1}. Electrochemical impedance spectroscopy (EIS) spectra containing 0.05 M vanadium species in 1 M sulfuric acid (PEIS - 0.26 *V* vs. SHE) was done at a frequency from 100 *mHz* to 200 *kHz*. The hydrogen-evolution reaction of all electrodes studied was evaluated using linear sweep voltammetry (LSV) at 2 mV s^{-1} in 1M H_2SO_4. Tafel measurements were done under potentiostatic control in a 50% SoC V^{3+}/V^{2+} and 1 M H_2SO_4 solution. In order to ensure it, potentiostatic -0.26 V was applied until the current is stable near 0 mA cm^{-2}. Afterwards, differentials of potential were applied in a range of ± 200 mV from the equilibrium (E_{ocv} = -0.26 V) to obtain j_0 which is directly related to the kinetics of the reaction.

2.6.Flow-Cell Test.

The electrolytes were prepared dissolving 1 M vanadium ions (Alfa Aesar) in 3 M H_2SO_4 (Aldrich, 98%) solutions. The corresponding anolytes and catholytes can be prepared through an electrochemical process[12]. The VRFB single-cell performance was measured using an in-house designed flow cell system, which has been described in our previous work [12]. The single-cell was assembled sandwiching the membrane (Nafion® 117, 6 cm × 6 cm) between two pieces of working electrodes with an area of 4 cm^2, approximately compressed a 30%. The graphite bipolar plates which are composed of 3

serpentines flow fields with diameter of 2 mm. The outer faces of the bipolar plate were coated with a sputtered layer of copper to act as a current collector. Viton® gasket was used to seal the cell. Metallic aluminium end-plates were used to close the cell. In order to investigate the effect of the different materials, nitrided TiO_2 nanorods have been used as negative electrodes, while CF-HT was used as positive electrode. The single-cell was connected to two glass reservoirs containing 20 mL catholytes and anolytes, respectively. The flow rate at each side was 10 mL min^{-1} and the negative reservoir was continuously purged with nitrogen to avoid any oxidation of the active species. The flow cell was charged up to 1.8 V and then discharged to 0.8 V, at different current densities, from 25 to 150 mA cm^{-2}. The performance evaluation method for the VRFB single cell was mainly determined by the following efficiencies: 1) Coulombic efficiency (CE), the ratio of the average discharging capacity to the average charging capacity, 2) Voltage efficiency (VE), the ratio of the average discharging voltage to the average charging voltage, (3) Energy efficiency (EE), VE multiplied by CE/100. According to Faraday's law, the theoretical capacity in VRFB was calculated to be 536 mAh (13.4 Ah L^{-1}) or 18.8 WhL^{-1} for 1 M vanadium ions concentration, respectively. The theoretical capacity expressed in AhL^{-1} has been calculated taking into account the total volume of the tanks (i.e. 40 mL). Additionally, to study the battery response to pulsed current and therefore plot the polarization curve, the battery was discharged at a specified current density, from 0 to 1900 mA cm^{-2}, for 60s. After, a rest period of 2 min to a steady state at OCP was measured. The power density curves were obtained from the product of output voltage at the voltage applied and the corresponding current density. These measurements were

performed at a 100% state of charge (SoC) as a starting point for each one of the current densities applied.

3. RESULTS AND DISCUSION

3.1. MORPHOLOGICAL AND STRUCTURAL CHARACTERIZATION

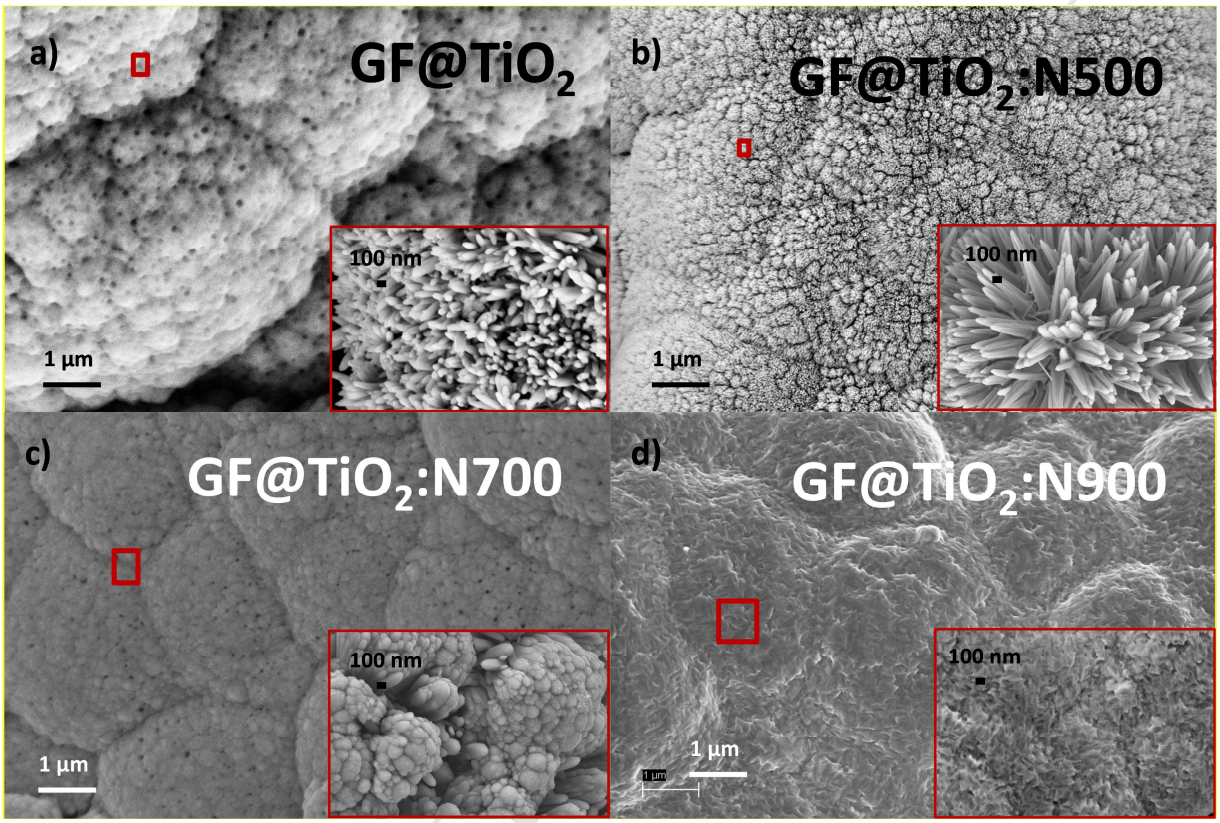

Figure 2- FE-SEM images of the: **a)** CF@TiO_2; **b)** CF@TiO_2 N500; **c)** CF@TiO_2 N700 **d)** CF@TiO_2 N900.

The morphological structures of the as-prepared electrode were characterized by FE-SEM. TiO_2 nanowire coverage directly growth into the surface of carbon felt, which is 0.45 m^2/g (**Figure S1**), with rod morphology by hydrothermal process (**Figure 2**) containing an average weight of 48% in titanium dioxide (**Figure S2**). Some changes can be appreciated after the NH_3 thermal treatment, which forms local agglomerations of TiO_2-nanorods due to the reductive conditions of the ammonia gas[44]. The initial nanorods size for the CF@TiO_2 electrodes, with a BET surface

area of 9.9 m^2/g, is smaller comparatively with those after thermal treatment at 500^oC. In this case the nanorods tend to be more compact and larger. However, as the temperature increases a sintering effect makes the particle size to diminish for 700^oC. In case of annealing at 900^oC the particle size and porosity of the covering layer is highly reduced, which is shown in the value of BET surface area with a value of 1.7 m^2/g.

Subsequently, the XRD spectra of the samples annealed at different temperatures (**Figure 3a**) showed an initial rutile (TiO_2) structure of the deposit over carbon felt with the diffraction peaks at 27.4, 35.8, and 54.38 θ, consistent with the rutile TiO_2 (110), (101), and (211) crystalline planes, respectively. All peaks were in line with the standard pattern (JCPDS: 21-1276). After the NH_3-treatment at 900ºC, three diffraction peaks appear at 61.8; 42.7 and, 37.2 2θ , which correspond to the (111), (200) and (220) planes of the cubic TiN phase (JCPDS: 65-0714). Below 900ºC as a temperature annealing, it can only be observed a broad peak due to the nitride process at 42.7 corresponding to (210) for the rutile phase. A more detailed analysis **(Figure 3b)** of the diffraction peaks associated with the rutile phase showed a distortion of the peak profile produced by the incorporation of nitrogen into the interstitial sites of rutile phase.

i) The rutile peaks show an asymmetrical shape indicated by the area patterned with a sparse green square, as **Figure 3b** shows around 36º. This corraborates that nitridation process due to the chemical interaction at the surface level is producing the breakage of the bonds in the TiO_2, producing a lattice weakness that leads to the generation of defects and vacancies and gives rise to a damaged outermost TiO_2 layer, which justifies the asymmetrical shape of the peaks, as the damaged area contributes essentially with larger interatomic distances, i.e. to the left area of the peaks[45].

ii) Secondly, the TiO_2 rutile structure remains even after the appearance of a cubic TiN phase around 900 °C pointing out that only a TiN formation. However, the position of the XRD pattern of the rutile peaks shifts towards higher 2θ values as the temperature is increased from 500 to 900ºC, i.e. from 27,58º to 27,71º showing that rutile had undergone a nitrogen doping over titanium dioxide nanorods as temperature was increased achieving strain values (Δd/d) around +1%, where "d" is the inter-planar spacing. The crystalline domain size from these XRD spectra considering Debye-Scherer formula is around 50 *nm*.

iii) Thirdly, as the nitrided treatment reaches 900 ºC, there is an overall modification of the sample structure. The broad peaks presented in the green area, observed in **Figure 3b,** disappear, showing that the stoichiometry of TiO_2 is recovered and TiN phase formed. Therefore, it is plausible to assume that TiN is localized at the outermost zone of the remain unaffected TiO_2, exactly where TiN stress phase formation can be relaxed. For this phase, the crystalline domain from the Debye-Scherer formula is around around 30 *nm*. Additionally, the XRD of CF@TiO_2N500 and CF@TiO_2N700 does not show any peak realated to TiN. In consequence, at this stage, TiN phase is not yet seggregated from the TiO_2 and nitrogen is only present inside of the TiO_2 lattice such as the peak deformation corraborates. It is also worth consider such high temperatures could also functionalize the carbon felt surface.

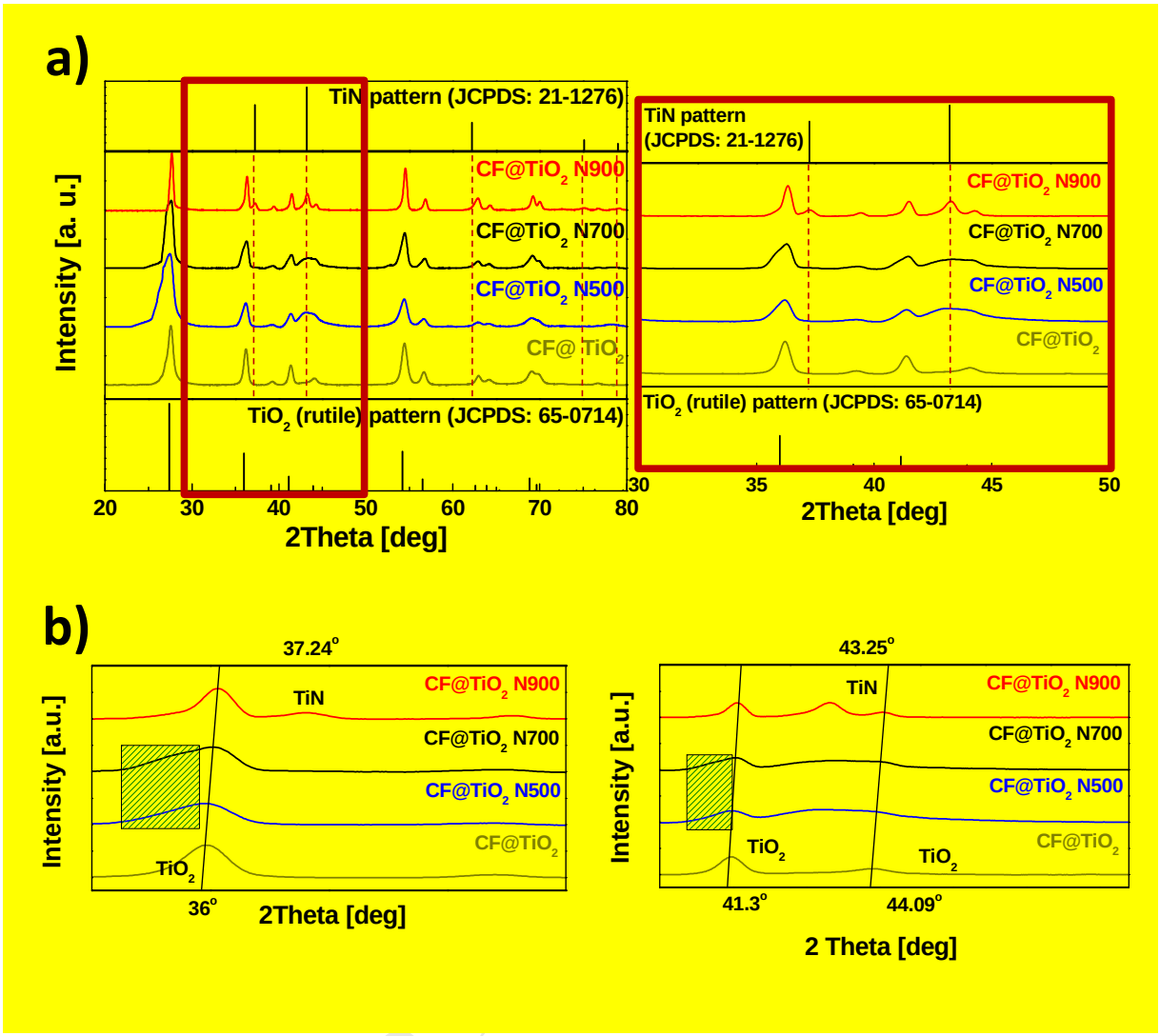

Figure 3- a) X-ray diffractogram of CF@TiO_2, CF@TiO_2 N500, CF@TiO_2 N700 and CF@TiO_2 N900 electrodes, showing chacteristic TiN (top) and TiO_2 (rutile, bottom) patterns. **b)** Detailed analysis of the XRD peaks showing the asymmetrical shape due to the nitrided process as well as the appeareance of the new TiN phase at 900ºC.

3.2.CHEMICAL CHARACTERIZATION

XPS spectra analysis (**Figure S3**) shows the surface effects of the nitride process. The influence of nitrogen incorporation on the state of titanium was probed through the Ti2p spectra (**Figure 4**). Significant differences can be distinguished for the CF@TiO_2 N900 sample, it can be seen that 3 doublets are needed to fit the titanium signal corresponding to the different expected bonds Ti-O (458.5 eV), Ti-N-O (456.8 eV) and Ti-N (455.9 eV) in a relative percentage of 50%, 29% and 21%, respectively. Comparatively the typical TiO_2 doublet related to titanium (IV) at 458.5 e eV is seen in CF@TiO_2 and CF@TiO_2 N500, with a small additional doublet contribution from Ti (III) in the lattice structure in case of CF@TiO_2 N500 at 458.9 eV.

Furthermore, the O1s spectra in **Figure 4** shows an increasing surface defect formation over the metal oxide lattice by oxygen deficient groups, Ti-O (dark blue peaks) at 531.5 eV, following the relative area percentage: CF@TiO_2 (22%) < CF@TiO_2 N500 (45%) < CF@TiO_2 N900 (51%). There is also the existence of small contributions related to different oxygen bonds over the carbon surface centered at higher energy values (533 eV) (light blue peaks). Oxygen XPS band for CF@N900 (**Figure S4**) gives evidence for the oxygen groups formed on the carbon felt surface, as three deconvolution peaks related to C=O (rel. 2%) at 530.8 eV, C-O (rel. 69%) at 532.1 eV and C-O-H (rel. 29%) at 534.2 eV

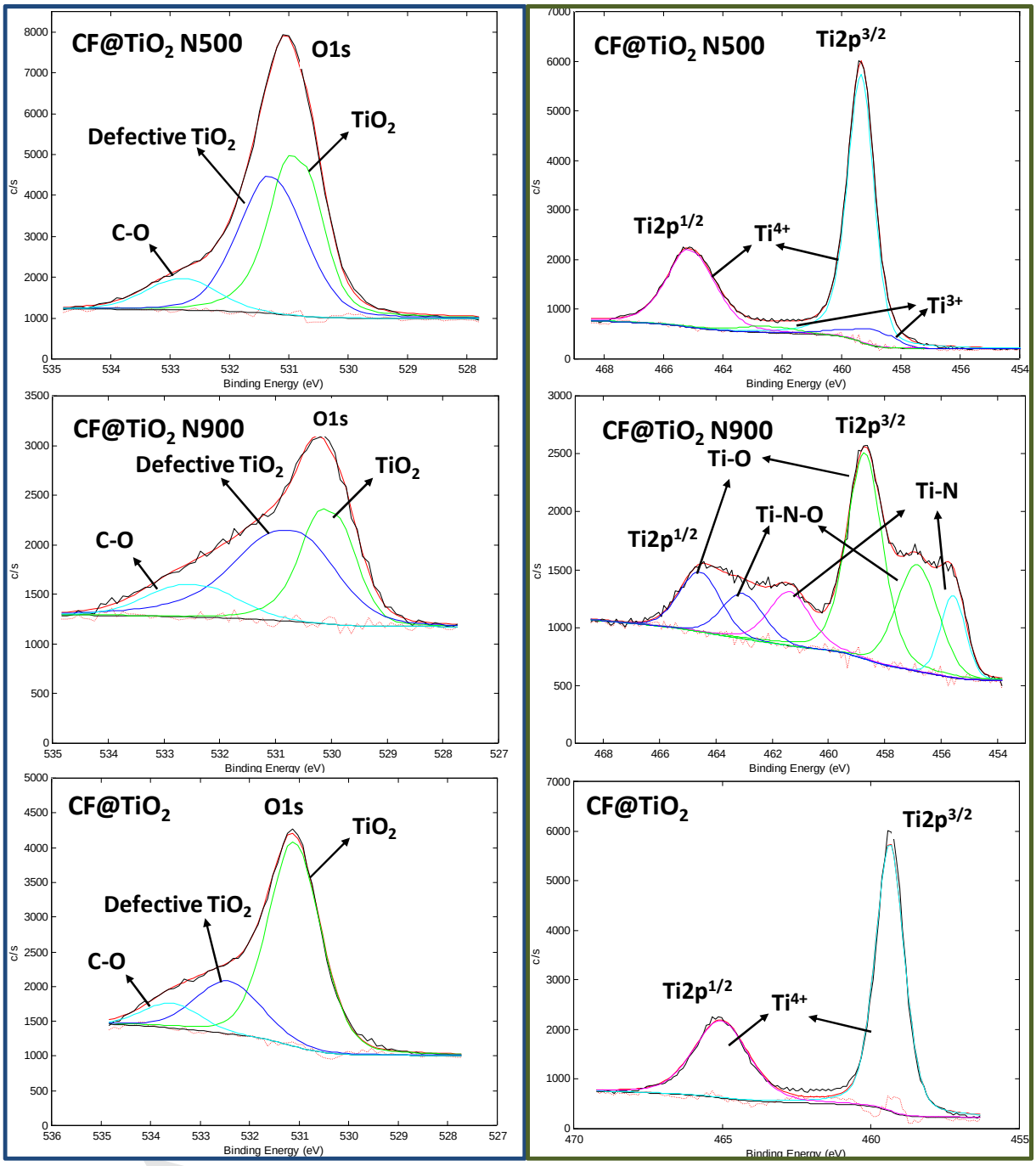

Figure 4- O1s and Ti2p XPS spectra for CF@TiO_2, CF@TiO_2 N500 and CF@TiO_2 N900.

Hence, bearing in mind that XPS signal is accurate for a few nanometers thickness (about 10 *nm*)[46,47], the crystalline domain determined from the XRD spectra the surface of CF@TiO_2 N900 electrode could be described as a TiO_2 surface with numerous zones of TiN (21%) surrounded by Ti-O-N transition areas between TiN and TiO_2 at surface level (29%). It is confirmed by the N1s XPS band spectra (**Figure S5**) that CF@TiO_2 N900 shows as main contributions the N-Ti (4% at.) bonding at 396 eV, as well as Ti-N-O (4% at.) at 398 eV, both centered at 396.1eV. Moreover, there is a 2% contribution of the spectra coming from pyridinic, pyrrolic and graphitic nitrogen groups formed at the carbon felt surface uncovered , which are centered at 400.2 eV. A 55% corresponds to pyridinic-N (399.7 eV), 31% to pyrrolic-N (400.3 eV) and 13% to graphitic-N (401.3 eV). The nitrogen functionalization is confirmed for CF@ N900, as the deconvolution of the high resolution N1s spectra reveals the presence of the peaks related to: pyridine-N (399.7 eV), pyrrole-N (400.3 eV) and graphitic-N (401.3 eV).

Furthermore, EDS mapping of a CF@TiO2 N900 fiber cross-section, as seen in **Figure S6**, have been done in order to elucidate where the TiN phase is located. Although the characterization technique cannot distinguish that scattering, XPS characterization showed the element composition on the electrode surface. This result is coherent with the TiN/TiO_2 ratio value obtained by TGA, which is 0.22. Considering the weight percentage for CF@TiO2 N900 there is a 12.6% of TiN in contrast with a 56.6% of TiO_2 (**Figure S2**).

The NH_3-treatment notably modifies the surface chemical states and, consequently, the optical properties of the TiO_2. For example, the color of the rutile's deposit, which is completely white in the case of the initial TiO_2 sample, (**Figure 5a**) turns bluish on the deposit after NH_3-treatment at 500^oC (**Figure 5b**), due to defect formation on the rutile[48],[49] caused by the reducing effects produced by the presence of ammonia. The annealed sample at 700^oC (**Figure 5c**) is

changed to black due to a deeper defect formation. Finally, the case of 900*ºC* (**Figure 5d**) turns to a brown color as a result of the titanium nitride (TiN) formation. The following reactions explain the annealing processes that the electrodes are subjected to in the presence of ammonia[50]:

$$2NH_3 \longleftrightarrow N_2 + 3H_2 \quad (4)$$

$$TiO_2 + H_2 \longleftrightarrow TiO + H_2O \quad (5)$$

$$TiO + NH_3 \longleftrightarrow TiN + H_3O^+ \quad (6)$$

$$TiO_2 + NH_3 \longleftrightarrow TiON + H_3O^+ \quad (7)$$

$$2TiO + N_2 \longleftrightarrow 2TiON \quad (8)$$

Initially, when ammonia gas is heated, it decomposes to hydrogen and nitrogen gas (4). Hydrogen partially reduces the titanium dioxide phase to titanium monoxide (5) which in the presence of the acidic electrolyte will form the oxyhydroxide. However, in order to produce titanium nitride, the heating temperature should reach at least 800 *ºC*. Below that temperature, reaction (6) will not take place; therefore TiN will not be formed. Intermediate reactions (7) and (8) take place from 700ºC to form the oxynitride phase[51].

In order to confirm these findings, the UV-vis spectra (**Figure 5e**), was performed in the as-prepared electrodes. TiO_2 nanorods after ammonia thermal treatment at 500^{o}C displayed a color change from white (CF@TiO_2) to blue (CF@TiO_2 N500).

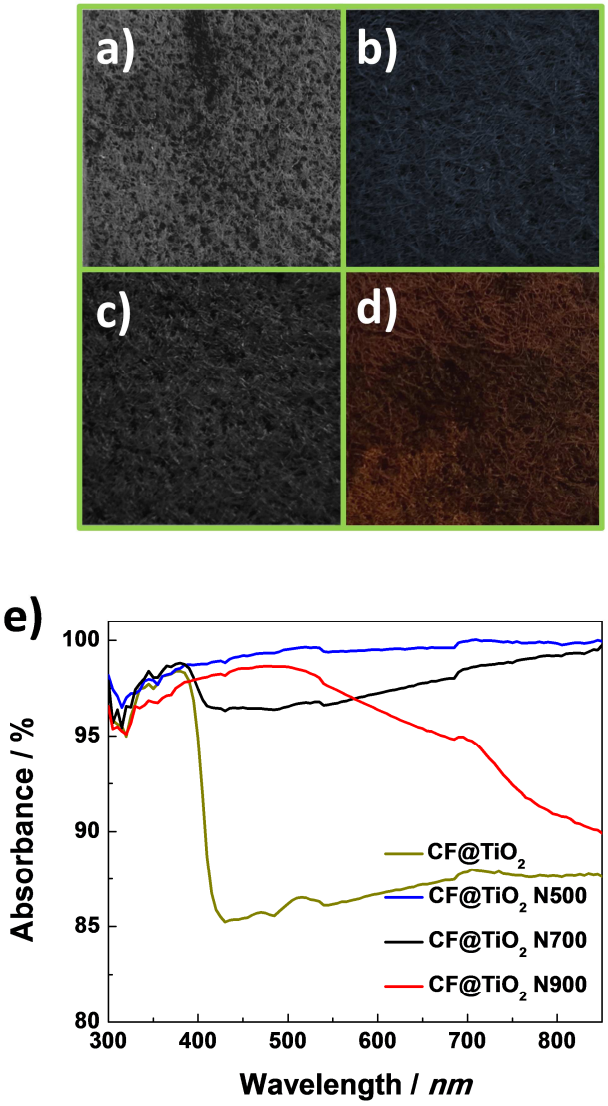

Figure 5- Images, taken from Carl-Zeiss optical lens, of the electrodes after their respectively treatment: **a)** CF@TiO_2; **b)** CF@TiO_2 N500; **c)** CF@TiO_2 N700 **d)** CF@TiO_2 N900 **e)** UV-vis Absorption spectra for CF@TiO_2, CF@TiO_2 N500, CF@TiO_2 N700 and CF@TiO_2 N900.

This suggested that CF@TiO_2 N500 electrode has an optical response in the visible range extending its absorption from UV into 800 nm (**Figure 5e**), in contrast to CF@TiO_2 electrode which only presents absorption in the UV region (< 400 nm). This expansion in the absorption from the UV to visible spectra could be attributed to oxygen vacancies formation in the titanium dioxide structure (bands at 441 and 486 nm), responsible for the changes in the electronic distribution, and therefore, the blue color[52,53]. Moreover, CF@TiO_2 N700 slightly reduces its absorbance due to the color change from blue to black in the near UV region, but preserves a similar absorbance profile as CF@TiO_2 N500. Additionally, two absorption peaks around 494 and 695 nm are also observed in CF@TiO_2 N900 electrode. The appearance of these two peaks are related to the formation of TiN crystallites and surface Plasmon resonance effect of TiN, respectively[54,55].

3.3.ELECTROCHEMICAL CHARACTERIZATION

After studying the chemical modification of the different electrodes, cyclic voltammetry (CV) was conducted to analyze the electrochemical performance of our electrodes towards V^{2+}/V^{3+} redox reaction (**Table 1**). Several electrochemical observations can be made from the CV (**Figure 6a**). It is clearly evidenced the poor electrocatalytic activity of the CF towards the negative reaction in VRFB, as large differential peak potential corresponding to the V^{3+}/V^{2+} redox reaction is observed. This irreversibility is due to the fact that the CF electrode promotes the HER over the V^{3+}/V^{2+} redox reaction. The presence of the TiO_2 electrocatalyst over the surface of the CF electrode largely prevented the HER and the oxidation and reduction peaks corresponding to the V^{3+}/V^{2+} redox reaction could be clearly observed. However, none of these peaks are no symmetrical and the obtained current density values are the lowest for all modified

electrodes tested. Further differences can be observed, when compare CF@TiO_2 N500 and CF@TiO_2 N900 electrodes, and are summarized below:

1) The highest current densities for both processes, oxidation and reduction, is displayed by CF@TiO_2 N900 electrode (i.e. I_{ox}= 24.01 mA/cm^2 and I_{red}= -27.67 mA/cm^2), which evidences the greater electrochemical conversion of the active species on its surface due to a larger electrochemical active surface area towards the V^{3+}/V^{2+} redox reaction.

2) The peak-to-peak potential separation (ΔE) and the ratio of the reduction peak and the oxidation peak current (I_{red}/I_{ox}) provide information about the reversibility of the redox process. For one-electron transfer reaction, the values for a reversible redox reaction are ΔE = 0.059 V and I_{red}/I_{ox} = 1 at 298 K. A slight difference of the ΔE values between both electrodes, CF@TiO_2 N500 and CF@TiO_2 N900, can be observed 0.24 and 0.22 V respectively. However, a significant increase from 0.60 to 0.87 for I_{red}/I_{ox} can be observed, showing a higher symmetry for CF@TiO_2 N900 electrode towards the reaction. Thus, in terms of electrochemical reversibility, the CF@TiO_2 N900 electrode presents better features, achieving values for a quasi-reversible reaction towards V^{2+}/V^{3+}.

Table 1 – Electrochemical values obtained from the cyclic voltammetry plots.

Sample	E_{ox} / *V*	E_{red} / *V*	ΔE / *V*	I_{ox} / $mAcm^{-2}$	I_{red} / $mAcm^{-2}$	I_{red}/I_{ox}
CF	**-0.066**	**-0.625**	**0.69**	**9.21**	**-13.98**	**0.66**
CF@TiO_2	**-0.228**	**-0.469**	**0.24**	**3.67**	**-6.84**	**0.54**
CF@TiO_2 N500	**-0.233**	**-0.468**	**0.24**	**5.28**	**-8.77**	**0.60**
CF@TiO_2 N900	**-0.232**	**-0.456**	**0.22**	**24.01**	**-27.67**	**0.87**
CF@N900	**-0.230**	**-0.463**	**0.23**	**15.95**	**-20.56**	**0.78**

Additionally, in order to elucidate the electrochemical influence of the nitrided process onto TiO_2 layer, as well as on the carbon felt, samples without TiO_2 layer were also prepared and analyzed, labeled as CF@N900. As observed in **Table 1**, the main differences between these two electrodes are observed in the current density values, the lower current density, from 33% for reduction to 25% for oxidation reactions, slightly smaller ΔE (0.23 V) and reduced I_{red}/I_{ox} (0.78) displayed by CF@N900 comparatively to CF@TiO_2 N900 electrode. It points out the positive benefit of the proposed technological route to enhance the VRFB negative redox reaction. Accordingly, the experimental data showed a synergetic effect between the nitrided process effect over the CF and on TiO_2 structure, coupling the better electron transfer towards V^{3+}/V^{2+}

redox reaction due to functionalization over the carbon electrode's surface and over the TiN nanocatalyst formed.

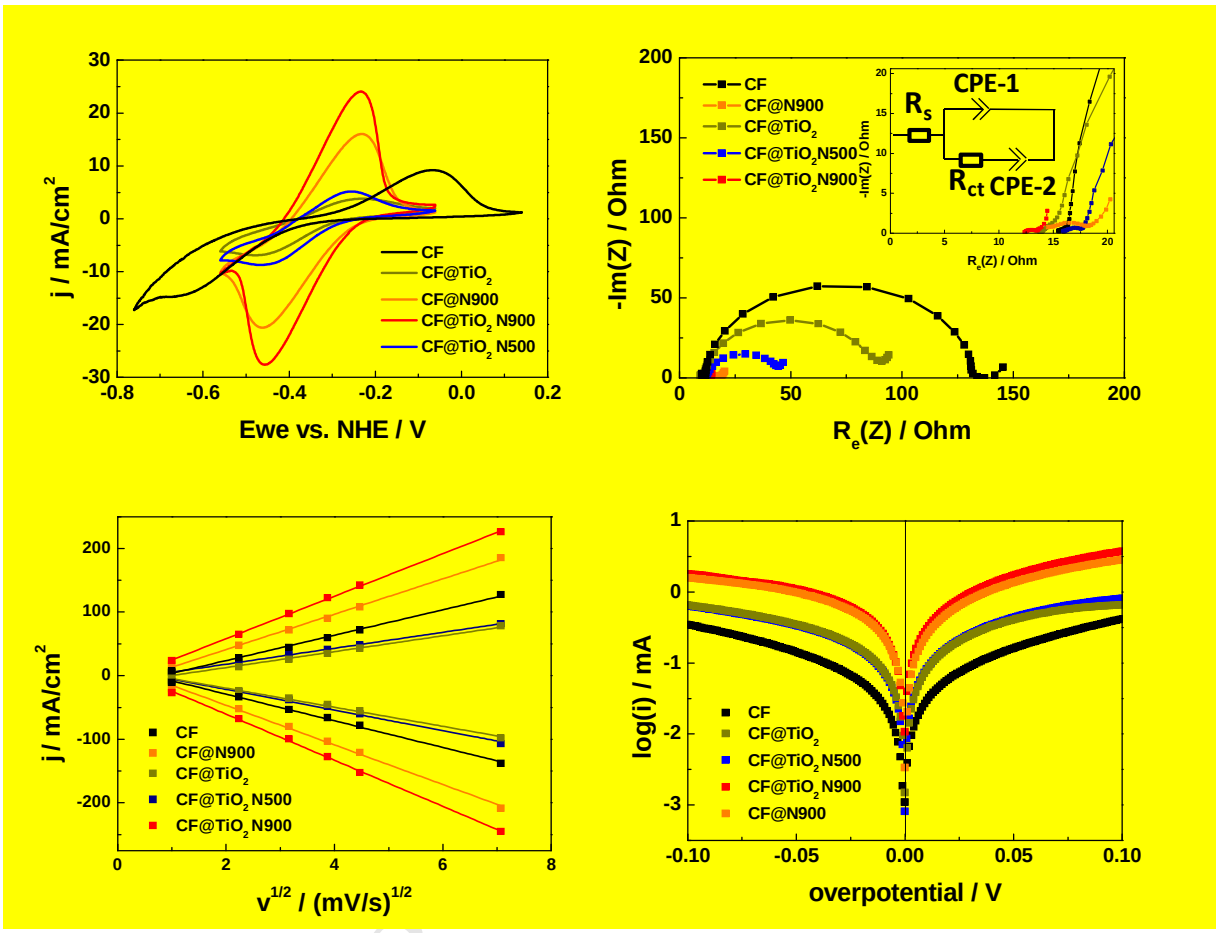

Figure 6 – a) Cyclic Voltammetry of the electrodes in 0.05 M $V^{3+}$and 1 M H_2SO_4 solution. The voltage was scanned negatively from E_{ocv} at 50% SoC (V^{3+}/V^{2+}) at a scan rate of 1 $mV\ s^{-1}$, to -0.56 *V* vs. SHE and after reversing the direction to an oxidative potential up to -0.06 *V vs.* SHE. **b)** Potentiostatic electrochemical impedance spectroscopy (PEIS) done at -0.26 V *vs.* SHE. **c)** Randles-Sevcik plot of *j* vs. $v^{1/2}$. **d)** Tafel plot log *i* vs. η (overpontential) for the different electrodes used in a 0.05 M 50% SoC V^{2+}/V^{3+} in 1 M H_2SO_4 solution.

Electrochemical impedance spectroscopy (PEIS) measurements were conducted for all the electrodes at -0.26 V *vs.* SHE, in order to establish the difference in the electrochemical behavior of the prepared electrodes. Nyquist plots (**Figure 6b**) of all electrodes a semi-circle at high frequency region and a sloped line at the low frequency region ascribed to charge transfer process and the diffusion process, respectively. The data were fitted using Randles equivalent circuit (**Figure 6b** onset). The following elements can be ascribed to the fitting: i) the R_s element represents the ohmic resistant, combining the electrolyte resistance, connection resistance, and the electrode resistance; ii) CPE-1 has a Faradic component (Y_1), which is a double layer capacitance (C_{dl}) of the interface between the electrode and the electrolyte, and a no-Faradic component (n_1), iii) charge transfer resistance (R_{ct}), and iv) CPE-2 has a Faradic component (Y_2), which represents the diffusion capacitance in pores of the electrodes, and a no-Faradic component (n_2). The data parameters obtained are listed in **Table 2** with an error less than 10%.

Table 2 – Parameters obtained from fitting the Nyquits plots with the equivalent circuit model of **Figure 6b**.

Sample	R_s / Ohm	CPE-1		R_{ct} / Ohm	CPE-2	
		Y_1 (C_{dl})	n_1		Y_2	n_2
CF@TiO_2	10.4	0.004451	0.92136	80.5	0.77467	0.81453
CF@TiO_2 N500	11.7	0.020095	0.89663	34.4	1.589	0.91352
CF@TiO_2 N900	12.3	0.084218	0.76553	1.25	2.781	0.6693
CF@N900	13.9	0.034198	0.61148	4.79	1.83	0.75279
CF	11.4	0.000322	0.97239	122	0.96348	0.58562

Consequently, CF@TiO_2 N900 sample has an electrochemical charge transfer resistance undeniably low (1.25 Ω) compared to the rest of electrodes. The formation of TiN phase highly

improves the charge transfer processes between the negative electrode and the vanadium ions, especially for CF@TiO_2 N900, as well as the presence of nitrogen groups at the surface of the carbon felt, as supported by XPS data (**Figure S4**). This makes CF@TiO_2 N900 the best performing electrode in this study, exhibiting a charge transfer resistance almost two orders of magnitude lower than CF@TiO_2[56]. It was also found that CF@N900 performed second best, due to the presence of N and O-groups over the carbonaceous surface, with an R_{ct} of 4.79 Ω. Moreover, C_{dl} values were found to follow the same trend as the R_{ct}, obtaining the larger value for CF@TiO_2 N900 (8.4 x 10^{-2} F) electrode due to higher amount of the active sites available for the reaction, which also agrees well with the CV analysis.

Besides, in cyclic voltammetry, the peak current, i_p, depends not only on the concentration and diffusion properties of the electroactive species, but also on the scan rate, as described by the Randles-Sevcik equation:

$$i_p = 0.4463nFAC\left(\frac{nFvD}{RT}\right)^{1/2}$$

Where i_p is the current maximum in Amps, n is the number of electrons transferred in the redox event (usually 1), A is the electrode area in [cm^2], F is the Faraday constant in [C mol^{-1}], D is the diffusion coefficient in [cm^2/s], C is the concentration in [mol/cm^3], v is the scan rate in [V/s], R is the gas constant in [J K^{-1} mol^{-1}] and T is the temperature in [K]. When a linear behavior is observed between the scan rate and the peak current for the redox couple V^{3+}/V^{2+}, the reaction is diffusion controlled. Prior to use this equation it is worth mention it is applied just as a qualitative approximation because it applies to reversible reactions and planar electrodes while the studied electrodes are porous and quasi-reversible reactions. In order to estimate the mass transfer the Randles-Sevcik equation is used [57]. The equation's plot (**Figure 6c**) gives us a

relationship where the slope is directly related to the associated mass transfer, which follows the trend: CF@TiO_2 N900 > CF@N900 > CF > CF@TiO_2 N500 > CF@TiO_2. These values evidence the higher mass transfer on the CF@TiO_2 N900 electrode towards the negative reaction, which is directly a consequence of a larger active area of the vanadium ions over the electrode and therefore being less diffusive limited. Moreover, the close value of CF@N900 to CF@TiO_2 N900 also evidences a facilitated mass transfer attributed to larger active area on the electrode's surface.

The Tafel equation was applied in order to confirm the catalytic properties of the different carbon felt modified electrodes (**Figure 6d**), which was mathematically treated and their values disclosed in **Table 3**. As seen, the exchange current density follows the trend (*mA*): CF@TiO_2 N900 (9.58×10^{-1}) > CF@N900 (6.87×10^{-1}) > CF@TiO_2 N500 (3.51×10^{-1}) > CF@TiO_2 (2.38×10^{-1}) > CF (6.6×10^{-2}). This is directly related to the equilibrium exchange current on the electrode towards the negative VRFB reaction. Therefore, the material prepared at the highest temperature (900 *ºC*) shows a superior electron exchange current with the electrolyte towards the redox reaction (V^{3+}/V^{2+}), which implies good catalytic behavior of highly nitrided electrodes. The heterogeneous rate constant was also determined, see **Table 3**, obtaining 1.6×10^{-3} cm s^{-1} for CF@TiO_2 N900 electrode one order of magnitude larger than CF@TiO_2 N500 electrode (5.8×10^{-4} cm s^{-1}). CF@TiO_2 N900 rate constant value is among the best values in the literature[23].

Table 3 – Exchange current density (i_0) values and heterogeneous kinetic rate constant obtained

from the Tafel plot in 0.05 M V^{3+} in 1 M H_2SO_4 at 50% SoC (V^{2+}/V^{3+}) for the electrodes CF, CF@TiO_2 and CF@TiO_2 N500, CF@TiO_2 N900 and CF@N900.

Electrode	I_0 / mA	k^0 /cm s^{-1}
CF	0.066	1.1 x 10^{-4}
CF@TiO_2	0.238	3.9 x 10^{-4}
CF@TiO_2 N500	0.351	5.8 x 10^{-4}
CF@TiO_2 N900	0.958	1.6 x 10^{-3}
CF@N900	0.687	1.1 x 10^{-3}

Comparatively, **Figure S7** shows at -0.26 *V* vs. SHE, the different slopes associated to the response time according to the proposed method by Fink *et al*[23] to determine the kinetic information for rough and non-planar electrode structures using a straightforward linear-relationship between the $1/R_{ct}$ and Cdl, both parameters obtained from EIS analysis (**Figure 6b**). According to this model, charge transfer resistance and double layer capacitance are related by the following equation:

$$1/R_{ct} = \frac{nFt_{dl}}{RT\varepsilon_r\varepsilon_0} j_0 C_{dl}$$

Where the variables correspond to the exchange current density j_0, the gas constant R, the absolute temperature T, number of transferred electrons n, Faraday constant F, relative dielectric permeability ε_r, permittivity of free space ε_0, and the thickness of the double layer t_{dl}. This indicates that R_{ct} decreases inversely with C_{dl} and that the slope of this equation yields the kinetic information j_0 (which is directly proportional to k^0).

Consequently, from the data shown in **Figure S7**, it can be observed CF@TiO_2 N900 possesses slightly faster kinetics than CF@N900, and significantly more than CF@TiO_2 500. Although the slope value is also included, the values referred to CF and CF@TiO_2 electrodes have a large error. The larger slope means a faster transition frequency towards the vanadium negative redox reaction, which is related to the kinetic constant (k^0), as the formula shown above. Therefore, the electrodes follow a kinetically favored trend as: CF@TiO_2N900 > CF@N900 > CF@TiO_2N500 > CF@TiO_2 > CF. The slope obtained by Fink's method (**Figure S7**) follows a linear relationship with the previously obtained values of k^0 by Tafel, evidencing the good behavior of the method.

Since the lower contribution of the parasitic reactions must be settled in order to assess a high Coulombic efficiency, as well as long lifespan of the electrodes performance, CV were performed in absence of any vanadium ion to study the HER on the surface of the different studied electrodes (**Figure S8**). The maximum current density values for the as prepared electrodes towards HER increases in the following order (mA cm^{-2}): CF@TiO_2 (89) < CF@TiO_2 N900 (150) < CF@TiO_2 N500 (180) << CF@N900 (248) < CF (258). There is a large inhibition of hydrogen evolution on the carbon felt covered by titanium dioxide as rutile phase, leading to a shift of the onset potential of HER, from -0.024 to -0.49 *V* vs. SHE[58]. The nitrided samples,

CF@TiO_2 N500 and CF@TiO_2 N900, also inhibited the HER compared to bare carbon felt, though not as strongly as before the nitridation treatment, -0.15 and -0.30 *V* vs. SHE onset potential for annealing at 500 and 900*ºC*, respectively. The inhibition of HER in this case was not as noticeable as in the case of pure titanium dioxide, due to the presence of fewer oxygen C-O centers, as demonstrated by XPS for TiO_2 and CF@TiO_2 N500 [29]. Moreover, CF@TiO_2 N900 exhibited a more negative onset potential compared to CF@TiO_2 N500 as the activation energy towards HER is comparatively larger. Last but not less important, CF@N900 increases the kinetics towards HER, in spite the fact that postpones the onset potential compared to CF. This result showed that the presence of TiO_2 does not inhibit H_2 formation and therefore, CF@N900 was not studied into a single cell.

3.4.SINGLE CELL PERFORMANCE

In order to assess the performance of the modified electrodes in a single cell, the carbon felt electrode incorporated with the nitrided titanium dioxide catalyst is used as the negative electrode in an all-vanadium redox flow cell, while for all the experiments treated carbon felt (CF-HT) was used as positive electrode. Several cell cycles at different current densities from 25 to 150 $mA\ cm^{-2}$ (**Figure S9**) were conducted in order to observe the effect of the current density on the cell capacity. Our carbon felt capacity drops dramatically from 12.6 $Ah\ L^{-1}$ at 25 $mA\ cm^{-2}$ current density to 3.3 $Ah\ L^{-1}$ at 100 $mA\ cm^{-2}$. However, it partially recovers its capacity when it is returned to the initial current density applied (10.9 $Ah\ L^{-1}$). On the contrary, the nitrided TiO_2 electrode retains the majority of their charge capacity from 13.1 and 13.6 $Ah\ L^{-1}$ at 25 $mA\ cm^{-2}$ to 9.8 and 10.1 $Ah\ L^{-1}$ at 150 $mA\ cm^{-2}$. This outstanding performance is a consequence of the synergetic catalytic effect of the oxygen and nitrogen sites on the carbon nitrided CF@TiO_2 over the adsorption, redox reaction and later desorption of V^{2+}/V^{3+} redox pair [34],[59].

Furthermore, the sample treated at 500 ^{o}C displays low voltage losses over the charge and discharge compared to the CF. However, this value was still higher than the cell with the nitrided electrode prepared at 900 ^{o}C. One of the main reasons for this result is the presence of TiN, coupled with the nitrogen and oxygen group formation on the carbon felt, which allows a reduced charge transfer resistance. As a consequence of this, during the charge-discharge at 150 $mA\ cm^{-2}$, the ohmic drop decreases, from CF@TiO_2 N500 to CF@TiO_2 N900 by 104 mV and 56 mV for charge and discharge respectively (**Figure S10**). As all components remained constant between tests, any differences on the system are due to the negative electrode. Therefore, the surface properties of the electrodes have a critical influence not only over the redox reaction kinetics, as previously shown, but also its ohmic resistance.

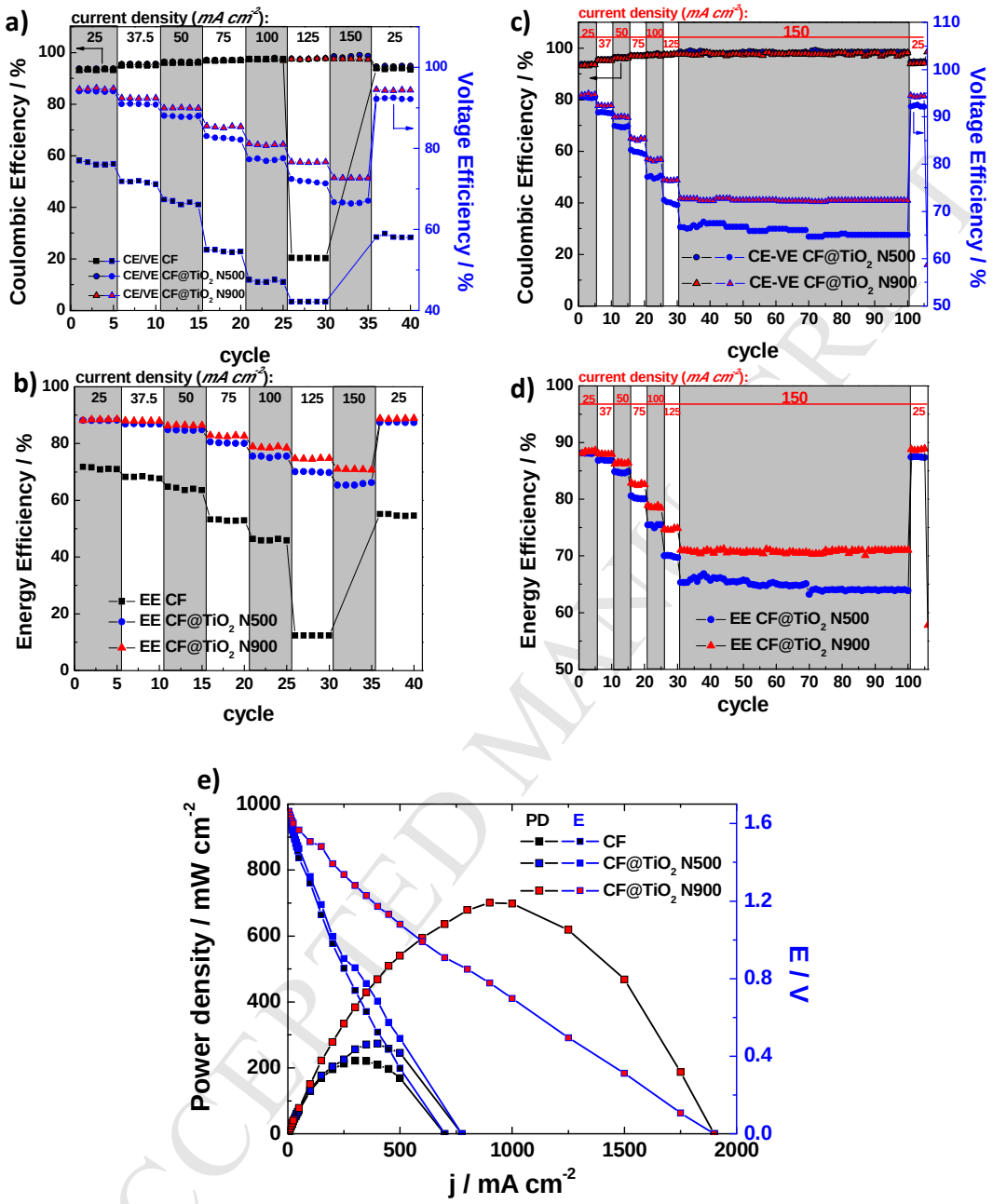

Figure 7 – a) CE and VE **b)** EE dependency with the applied current density (from 12.5 to 150 *mA cm*$^{-2}$) of CF, CF@TiO_2 N500 and CF@TiO_2 N900 as electrodes, for 1M of initial vanadium ions and 3 M H_2SO_4 as electrolyte. Single cell long-term cycling of the CF@TiO_2 N500 and N900 electrodes for 1M vanadium ions and 3 M H_2SO_4. **c)** Coulombic Efficiency (CE) and Voltage Efficiency (VE) ; **d)** Energy Efficiency (EE). **e)** Power density plot vs. current density for the electrodes CF, CF@TiO_2 N500 and CF@TiO_2 N900.

Subsequently, **Figure 7a and b** presents the Coulombic, Voltage and Energy efficiency for the electrodes CF, CF@TiO_2 N500 and CF@TiO_2 N900 respectively, as we cycle with current densities from 25 to 150 $mA\ cm^{-2}$. The sample annealed at 900^oC shows smaller losses as the current density is increased, and therefore a higher efficiency. A maximum energy efficiency of 86.5% is seen at the lowest current density (25 mA cm^{-2}), dropping to 71% at 150 $mA\ cm^{-2}$. We attribute the lower values compared to the state of the art in the literature[30] to the difference in cell set-up design and conditions. Nevertheless, it is clear that the coating of nitride TiO_2 on the surface of the graphite felts has a drastic improvement on performance of the cell compared to bare CF, under the same experimental conditions. Similarly, the decrease in energy efficiency for CF@TiO_2 N500 is markedly less than for the CF, where the efficiency decays abruptly when the current density applied increases. Especially up to 100 $mA\ cm^{-2}$, where the value collapses due to large overpotential, as seen in **Figure S11d**. The voltage efficiency, which is the ratio of charge and discharge voltage, follows the same trend as the Energy efficiency, a consequence of being the limiting factor of the battery performance. The Coulombic efficiency shows similar values for all samples (**Figure S11**), of above 95% for all current densities, except for the bare CF, due to an enormous overpotential at current densities above 100 mA cm^{-2} that causes a Coulombic efficiency drop approximately 20%. As HER increases, the overpotential also increases (**Figure S11d)**, causing critical imbalances between charge and discharge process. This provokes the system to fail when bare CF is used as negative electrode. Moreover, **Figure S11** shows the voltage profiles between 0.8 and 1.8 V for carbon felt, CF@TiO_2 nitrided at 500 ^oC and 900 ^oC, applying increasing current densities. It is obvious that the bare CF exhibited a larger ohmic drop than the nitrided electrodes, especially when compared to CF@TiO_2 N900, exhibiting

remarkably low polarization at high currents densities. There is a clear logarithmic tendency of the overpotential with increasing the current density (**Figure S11d).**

Thus, the nitrided catalysts annealed at 500 and 900*ºC* exhibited a stable cycling performance above 100 cycles at different current densities with more than 50 cycles at high-current (150 *mA* cm^{-2}). Nitrided CF@TiO_2 displays an initial Energy efficiency of 88.9% and 87.2%, for 900 and 500ºC annealing temperature, respectively. After 100 cycles, which is the largest stability reported up to date for these materials, corresponding to 2-3 weeks of cycling, the enhancement of CF@TiO_2 N900 achieved a stable cycling energy efficiency of 71.2% at 150 *mA* cm^{-2} compared to 63.9% energy efficiency for CF@TiO_2 N500. Therefore, we have demonstrated that there is a significant enhancement in the electrode performance, especially at high current densities, due to the significantly reduced polarization by increased redox active sites towards vanadium ions for the fast charge and mass transfer, which is consistent with all the electrochemical data previously shown. Following cycling at increased current densities, the system was returned to a charge-discharge rate of 25 *mA* cm^{-2}, in order to evaluate the catalyst stability (**Figure 7c and d**). Remarkably, the initial energy efficiency was recovered after cycling at high current densities, indicating an electrochemical and chemical robustness of nitrided CF@TiO_2 catalyst in concentrated acidic and high current conditions. Moreover, Coulombic efficiency and voltage efficiency values were the highest for CF@TiO_2 N900 samples. Nitrided CF@TiO_2 catalyst was shown to exceptionally enhance the electrochemical performance of the VRFB system. In fact, CF@TiO_2 N900 induces a fast charge transfer and vanadium ion adsorption, resulting in a high rate capability at 150 *mA* cm^{-2} and excellent capacity retention. This outstanding performance is a consequence of the synergetic catalytic

effect of the oxygen and nitrogen sites on the nitrided carbon felt and TiO_2 over the adsorption, redox reaction and later desorption of V^{2+}/V^{3+} redox pair [34],[59].

In fact, the observed improved performance in the electrode's mass and charge transfer, low ohmic resistance, as well as, limiting current density enables CF@TiO_2 N900 material to reach a superior power density, which is coherent with the electrode reaching a superior current values in the CV, previously shown in **Figure 6a**. The value of power density obtained, 700 $mW\ cm^{-2}$, is two and a half times higher than when annealed at 500°*C* and three times more than carbon felt electrode. The shape of the polarization curves (**Figure 7e**) shows that the maximum current density supply by the device is increased by two effects: i) a low ohmic drop as the current density is increased and ii) faster vanadium mass transfer, allowing larger amounts of vanadium to be polarized over the electrode surface as the power density increases. The voltage decay is much smoother in the case of CF@TiO_2 N900 electrode. It reaches a greater maximum power, while the other samples show abrupt voltage decay and significantly lower maximum power density. Therefore, the modified carbon felts (CF@TiO_2 N900) have enhanced the electrochemical performance of the negative electrode in all-vanadium redox flow batteries and, more importantly, the power density, which is usually insufficient in flow batteries technology.

3.5.MECHANISM PROPOSED

Based on previous research[60] and implementing the presented results, the mechanism proposed for the electrodes used is shown in **Figure 8a and b**. Firstly on bare CF, V^{3+} ions are adsorbed over the oxygen groups, -OH and C-O, on the carbon felt surface, generating O-V bonds, which breaks a O-H bond in the case where it is adsorbed on the

hydroxyl group and releases a proton to the solution. Consequently, an electron is donated to the V^{3+} reducing it to V^{2+} and breaking the previously formed bond (O-V) and taking the proton again from the solution to re-form the hydroxyl groups. In this case, this redox reaction competes with the hydrogen evolution reaction as the protons are easily adsorbed to the C surface to form an H-H bond and subsequently desorbed as H_2. The former reaction is kinetically more favourable, causing electrolyte imbalance and low performance. The inhibition of the HER is therefore an important factor in catalyst performance, as well as the enhancement of the V^{3+}/V^{2+} redox reaction.

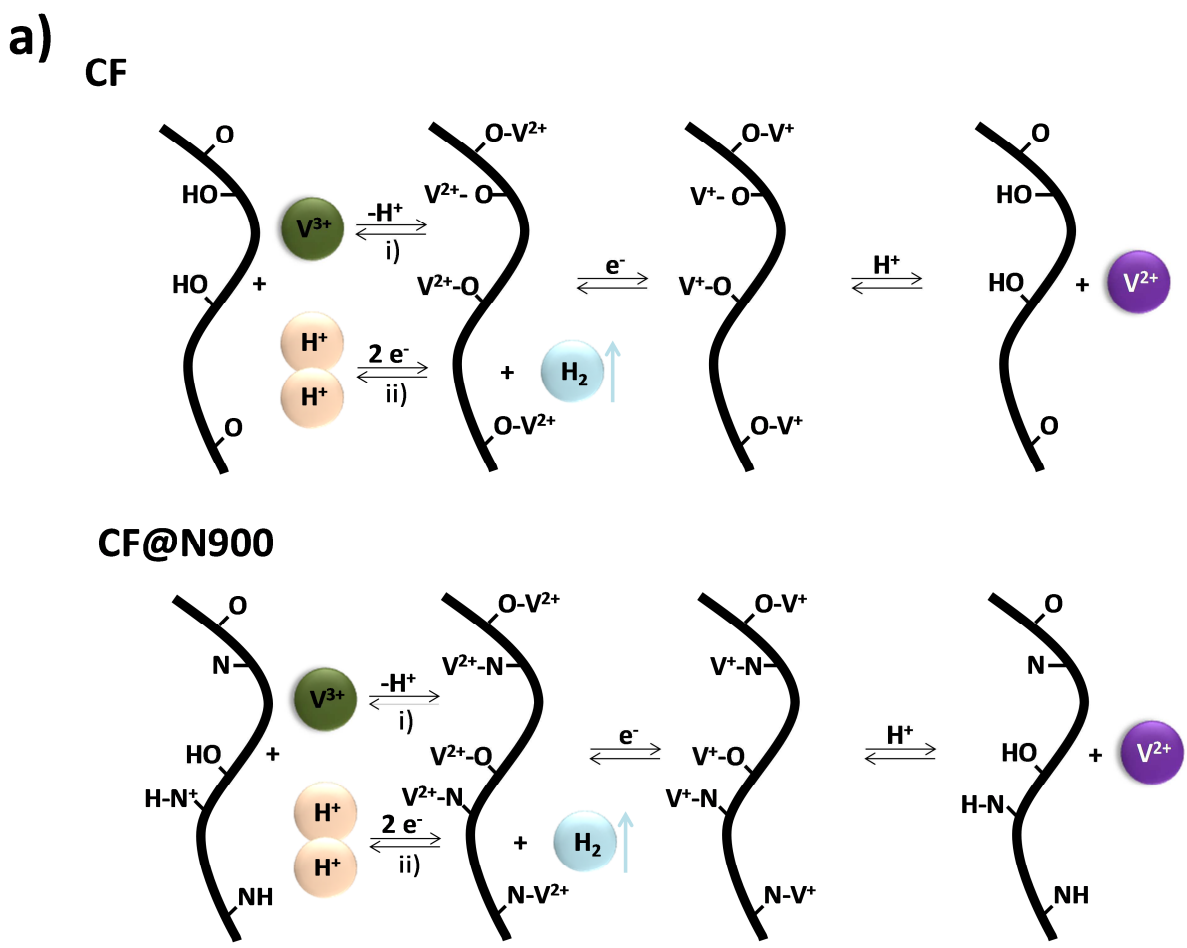

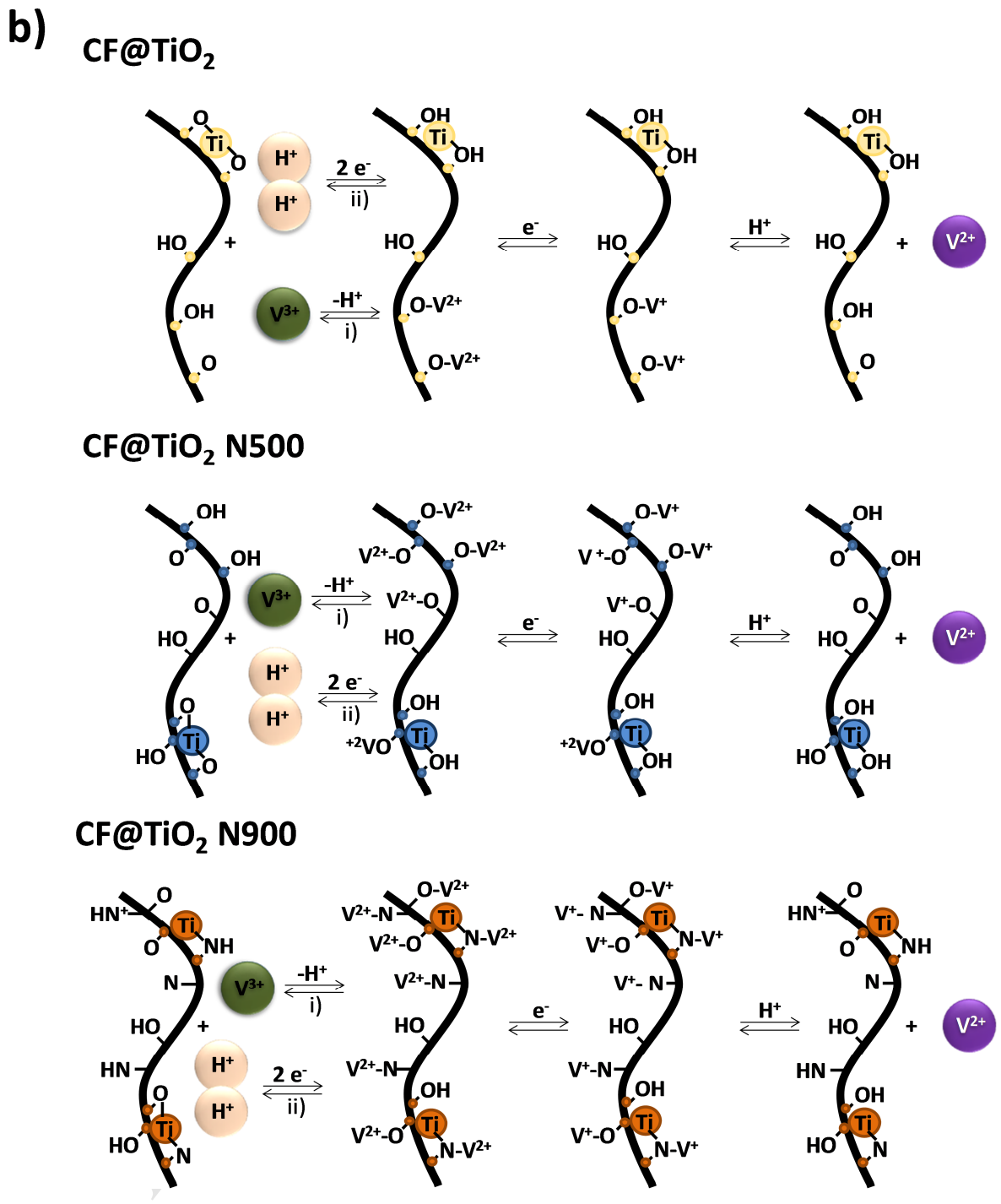

Figure 8. – a) Mechanism interpretation, based on published results[60], for the negative reaction of VRFBs using CF and CF@N900 electrodes. **b)** Mechanism interpretation, based on published results[60], for the negative reaction of VRFBs using CF@TiO_2, and nitrided CF@TiO_2 as electrodes.

In the case of CF@N900, V^{3+} ions are adsorbed over the oxygen (-OH and C-O) and nitrogen (pyridinic, pyrrolic and graphitic-N) groups on the carbon felt surface, generating O-V and N-V bonds, which breaks a O-H, N-H, $^{+}$N-H bond in the case where it is adsorbed on the hydroxyl, pyrrolic or graphitic group, respectively, releasing a proton to the solution. Consequently, an electron is donated to the V^{3+} reducing it to V^{2+} and breaking the previously formed bond and taking the proton again from the solution. This redox reaction also competes with the hydrogen evolution reaction for the same reasons as with the[61].

Thirdly, after the TiO_2 is deposited there are two conditions that favour the V^{3+} reduction: i) Increase of –OH groups and less importantly –O groups, as XPS data shows, due to the presence of titanium dioxide itself that promote the number of active sites per area for the reaction to happen, enhancing the electron charge transfer at the electrode/vanadium interface. ii) Highly stable proton absorption over the Ti-O bond inhibiting the HER side reaction. However, large electrode polarization is dominant at high rate capability leading to a limited specific capacity and a modest electrolyte-utilization ratio (SoC).

Consequently, the partially reduced sample (CF@TiO_2 N500) favours the V^{3+}/V^{2+} due to a reduced charge transfer resistance as an increased number of oxygen active sites (-OH and -O), especially hydroxyl groups, are present on the surface (**Figure 4**), and therefore, more vanadium ions are capable of react simultaneously.

Finally, for the sample where TiN is partially formed (CF@TiO_2 N900) there are two conditions that favour the V^{3+} reduction[62]: i) Increase of –N groups on the carbon felt

and over the TiO_2 surface forming TiN, due to the nitride process that promotes the number of active sites, enhancing the electron charge transfer at the interface electrode/vanadium. ii) Increase of oxygen groups, especially hydroxyl electroactive sites (-OH) over the electrode surface, for which electron charge transfer is facilitated by the nitrogen groups, most favoured by pyrrolic-N[63,64].

4. CONCLUSIONS

We have demonstrated that a novel negative electrode material, CF@TiO_2 N900, exhibited significantly enhanced performance for VRFB applications, with power density values of up to 700 $mW\ cm^{-2}$ based on nitrided TiO_2 decorated carbon felt. Samples were prepared by a simple and scalable two-step approach based on a first hydrothermal step for TiO_2 carbon felt decoration, followed by a high temperature nitriding step of 4 hours at 900^oC (after 4 hours at 500ºC under oxygen).

Furthermore, the reaction kinetics and reversibility of the negative electrode, V^{3+}/V^{2+} redox couple, showed an outstanding improvement when the nitridation treatment is conducted at 900ºC, CF@TiO_2 N900. the electrode CF@TiO_2 N900 showed an improvement of more than 310% in its associated kinetic constant rate, k_0, compared to carbon felt decorated with TiO_2, and an increase of 176% in relation to the TiO_2 decorated carbon felt nitrided at 500ºC. The partial transformation of TiO_2 to TiN takes place at the same time than the nitridation of the carbon felt itself occurs. From the potential catalytic properties of the three types of nitrogen groups (quaternary, pyrrolic and pyridinic), graphitic-N or quaternary-N is considered to be the more stable in the acidic environment. However, it is the pyrrolic-N group that is responsible for the

enhancement of the catalytic activity. These effects are coupled to the presence of oxygen groups, especially hydroxyl active sites. The incorporation of O and N-containing groups has been determined to be a key step due to substantial improvement of the electrochemical activity (i.e., higher current density, low oxidation-reduction differential of potential and higher reversibility).

Additionally, it enhances catalytic activity at the surface which makes both, the electrochemical V^{2+} oxidation and V^{3+} reduction reactions more favorable and faster on these electrodes for which apparent kinetic constant rates as high as 10^{-3} *cm* s^{-1} have been observed. These kinetic characteristics have also been corroborated by analyzing the electrochemical impedance spectra from where the deduced charge transfer resistance values decrease almost two orders of magnitude between the reference CF@TiO_2 and the sample treated at 900 *ºC*, corroborating the suitability of these electrodes for working stably at high density currents. These effects on the electrode behavior have also been shown with a reduction of the overpotential when large current densities are applied according to the Tafel plots. Likewise, this enhancement of the heterogeneous electron transfer kinetics, for V^{3+}/V^{2+}, has a significant impact on the current lost due to the parasitic HER, greatly decreasing it and contributing to an increase of the faradic efficiency.

Finally, the tested cell exhibits high coulombic, voltage, and energy efficiencies at different charge-discharge current densities, achieving more than 70% energy efficiency at 150mA cm^{-2}. Consequently, the reported procedure gives rise to electrodes with a large active surface area due to abundant oxygen functional groups and N-modified surface for vanadium active sites, which also reduces the charge transfer resistance. Compared with the electrode surface in absence of nitrogen, or a low concentration of it, the treated electrodes exhibit excellent catalytic activity

towards vanadium redox reactions also due to the enhanced rate of electron transfer through the nitrogen groups producing fast kinetics for vanadium ion transfer. Moreover, the battery with the proposed electrode has demonstrated an excellent stability and high capacity retention during the cycling test. Herein, the proposed energy storage system is capable of an improvement, supplying around 250% higher power compared to non-treated CF.

In summary, this work shows for the development and study of the electrocatalytic properties of highly active and stable nitrogen-modified carbon-based materials for VRFB applications, showing a synergetic effect of O- and N- functional groups at the surface of the carbon felt and the presence of TiO_2 / TiN. .

ASSOCIATED CONTENT

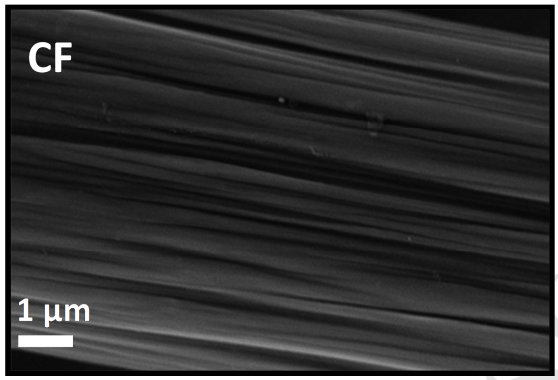

Figure S1. SEM image of carbon felt used as electrode, which has been treated.

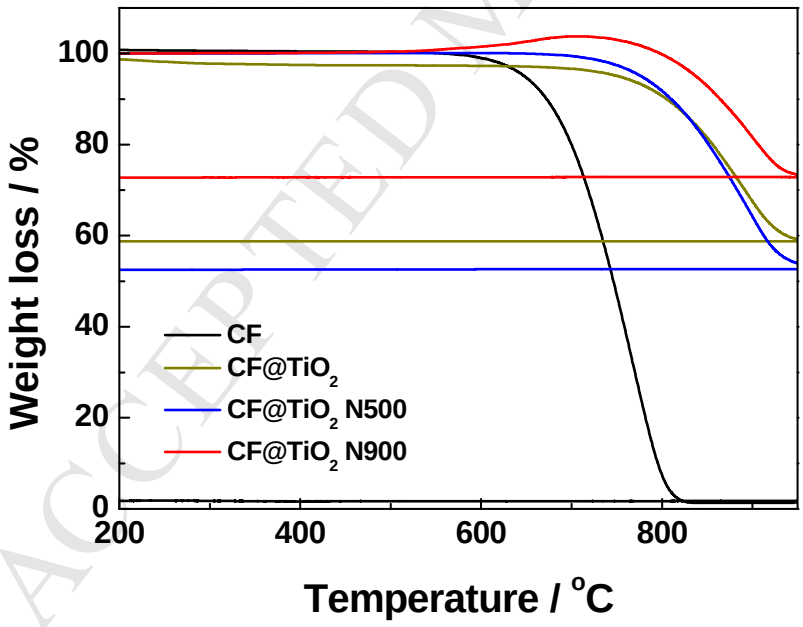

Figure S2. TGA done for different modified carbon felt electrodes, CF, CF@TiO_2, CF@TiO_2 N500 and CF@TiO_2 N900.

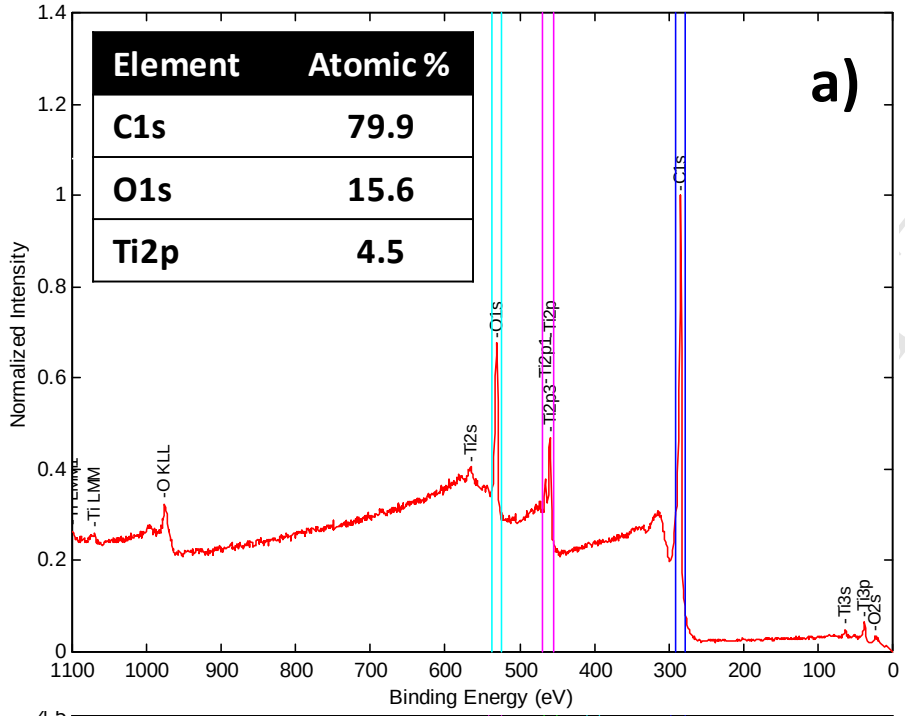
a)
Element Atomic %
C1s 79.9
O1s 15.6
Ti2p 4.5
Normalized Intensity
Binding Energy (eV)
- Ti LMM
- O KLL
- Ti2s
- O1s
- Ti2p3 - Ti2p1 Ti2p
- C1s
- Ti3s
- Ti3p
- O2s

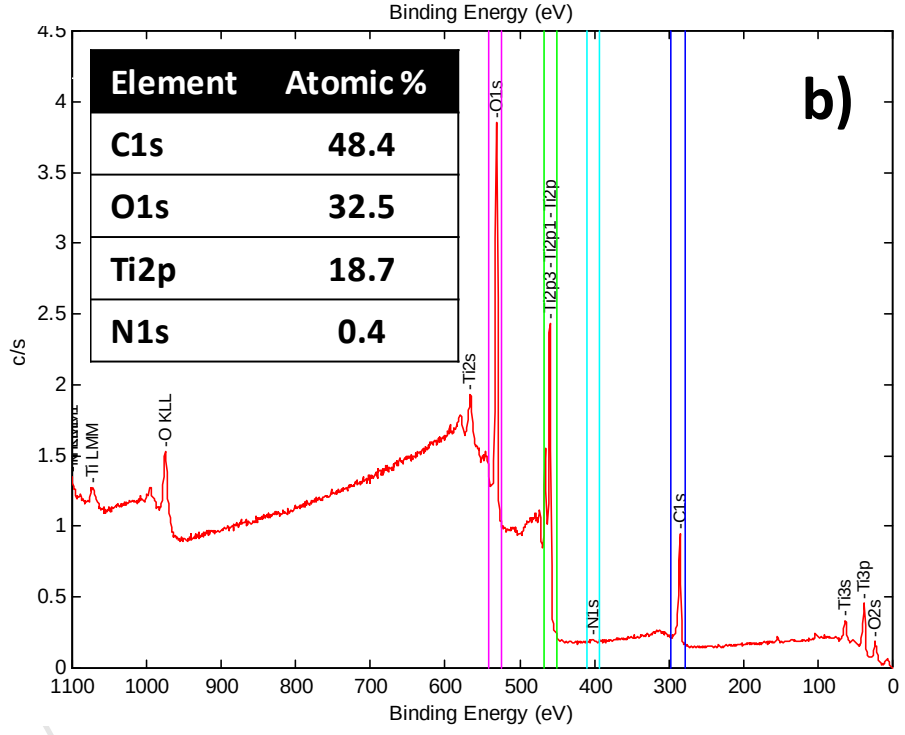
b)
Element Atomic %
C1s 48.4
O1s 32.5
Ti2p 18.7
N1s 0.4
c/s
Binding Energy (eV)
- Ti LMM
- O KLL
- Ti2s
- O1s
- Ti2p3 - Ti2p1 - Ti2p
- N1s
- C1s
- Ti3s
- Ti3p
- O2s

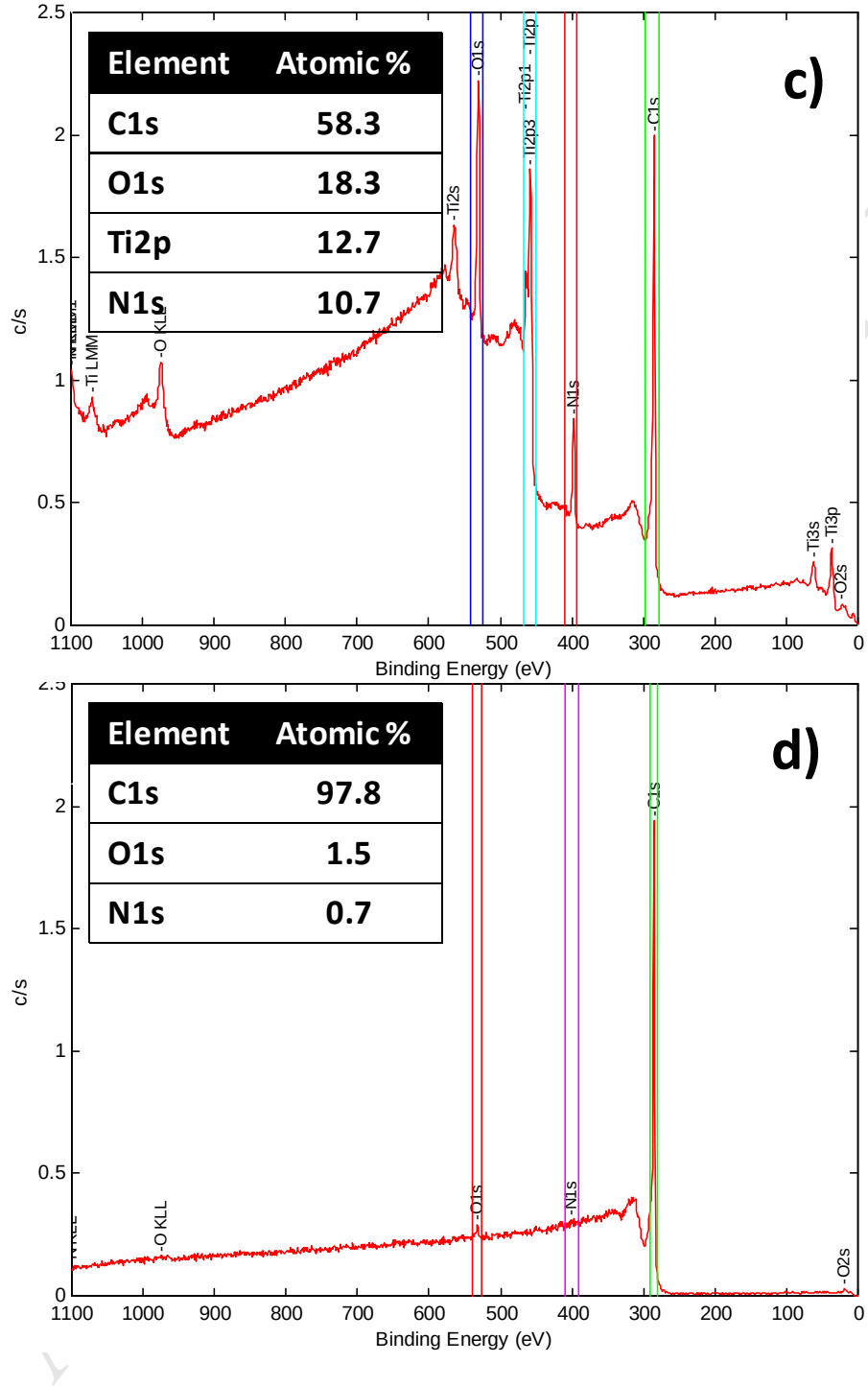

Figure S3. XPS general spectra **a)** CF@TiO_2 **b)** CF@TiO_2 N500 **c)** CF@TiO_2 N900 and **d)** CF@N900.

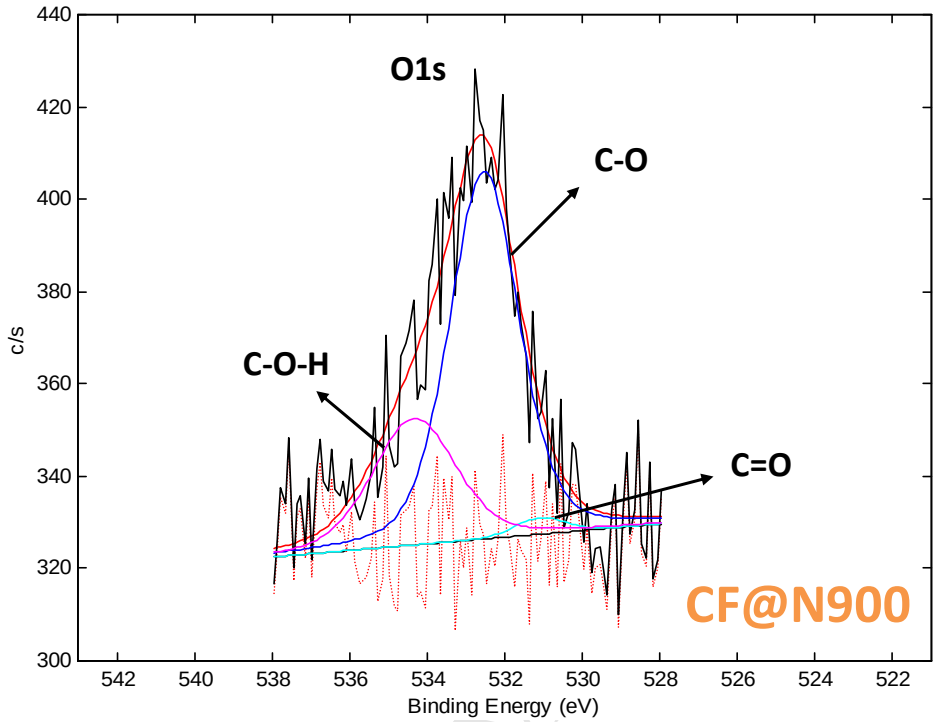

Figure S4. - XPS O1s band spectra deconvolution for the sample CF@N900.

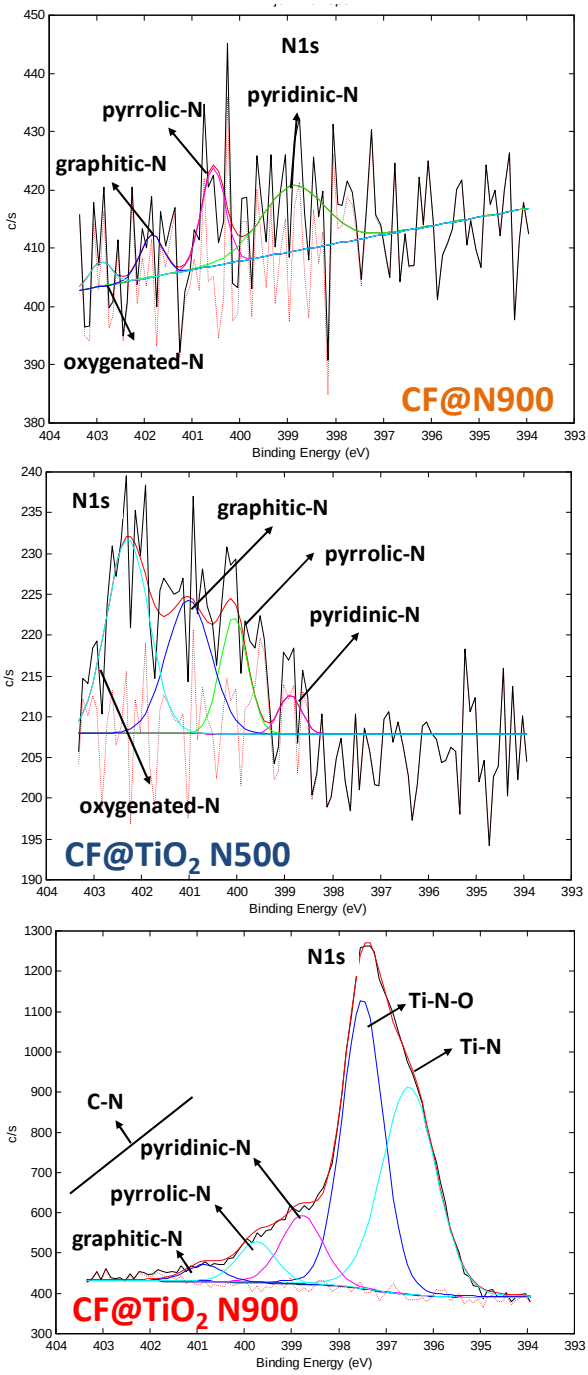

Figure S5. - XPS N1s band spectra for the samples CF@N900, CF@TiO_2N500 and CF@TiO_2 N900.

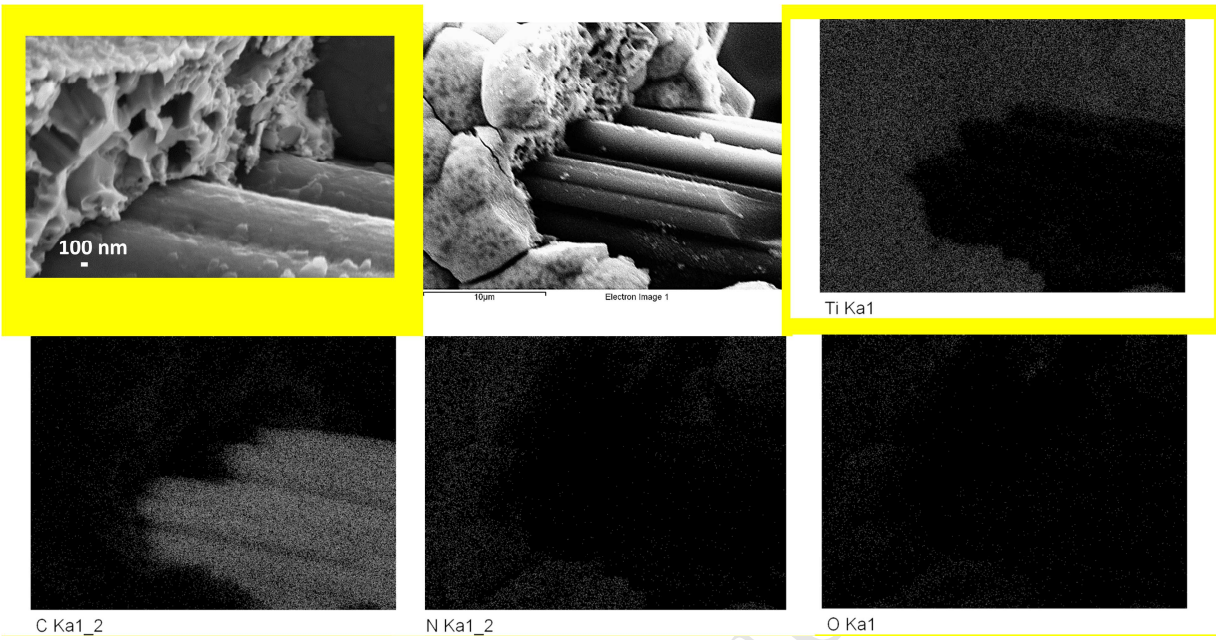

Figure S6 – SEM image and EDS mapping showing the Ti, C, N and O scattering of a CF@TiO2 N900 fiber cross-section

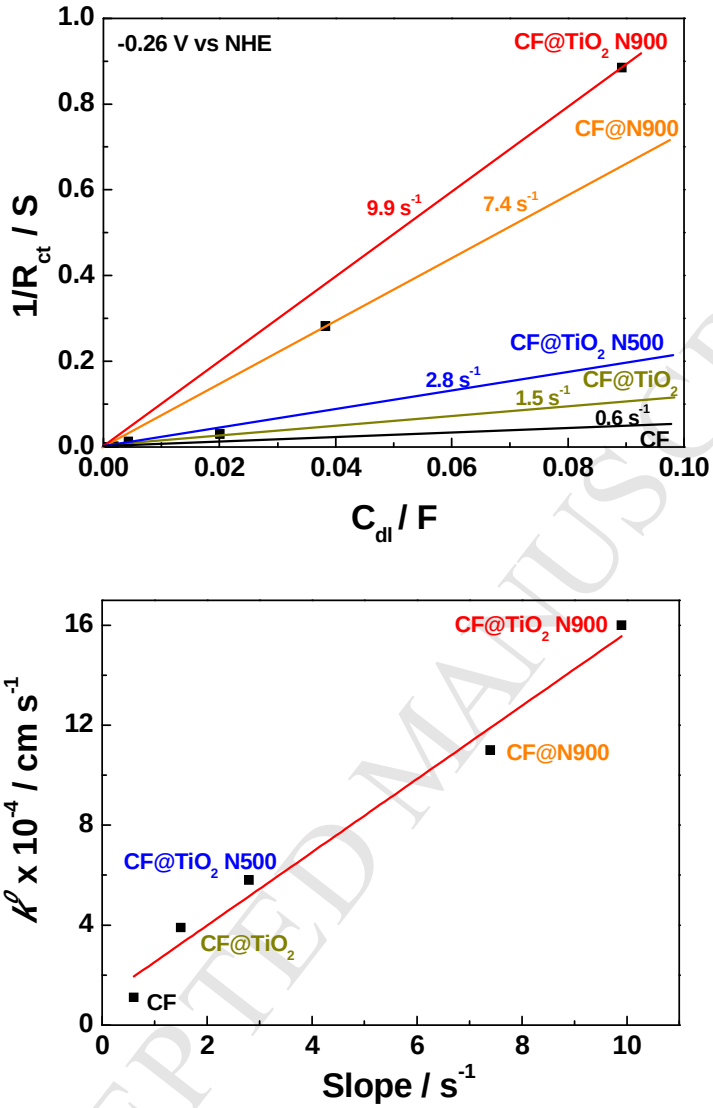

Figure S7 – Top. Plot of inverse of the charge transfer resistance ($1/R_{ct}$) vs. Capacitance of the double layer on the electrode surface (C_{dl}) for the different electrodes used at -0.26 V vs. SHE. **Bottom.** Linear relationship between k^0 Tafel values and slope obtained by Fink method.

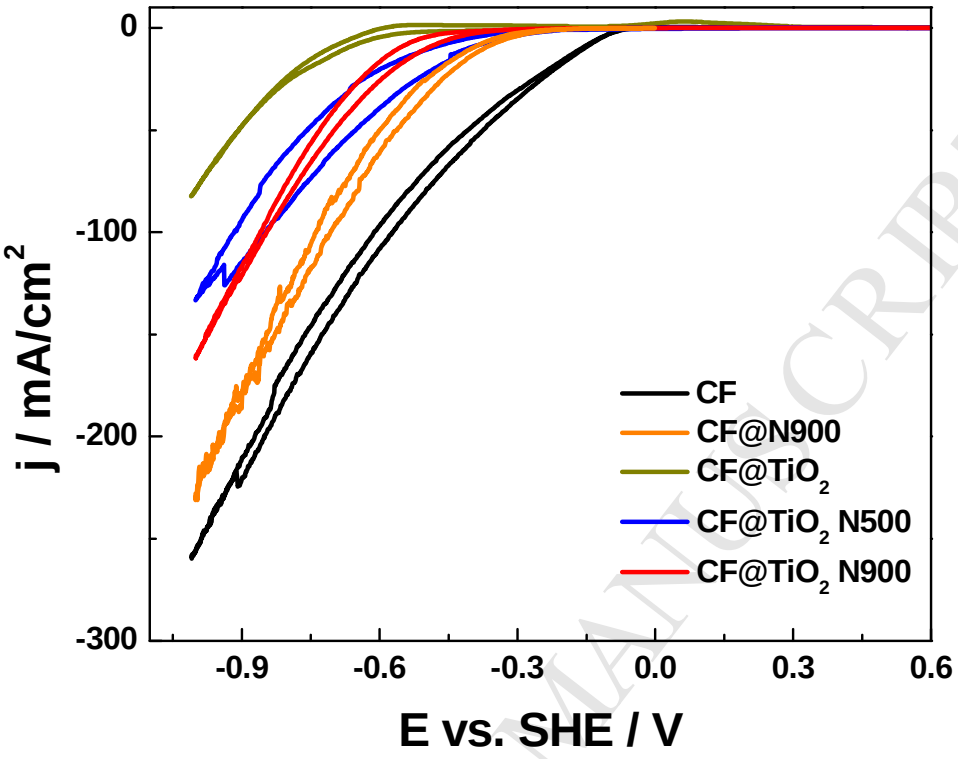

Figure S8 - Cyclic voltammetry (CV) of carbon felt, CF@TiO_2 and CF@TiO_2 N500 and N900 electrodes using a 1M sulphuric media at 2 $mV\ s^{-1}$, with potential window of 0.6 to -1 *V* vs. SHE.

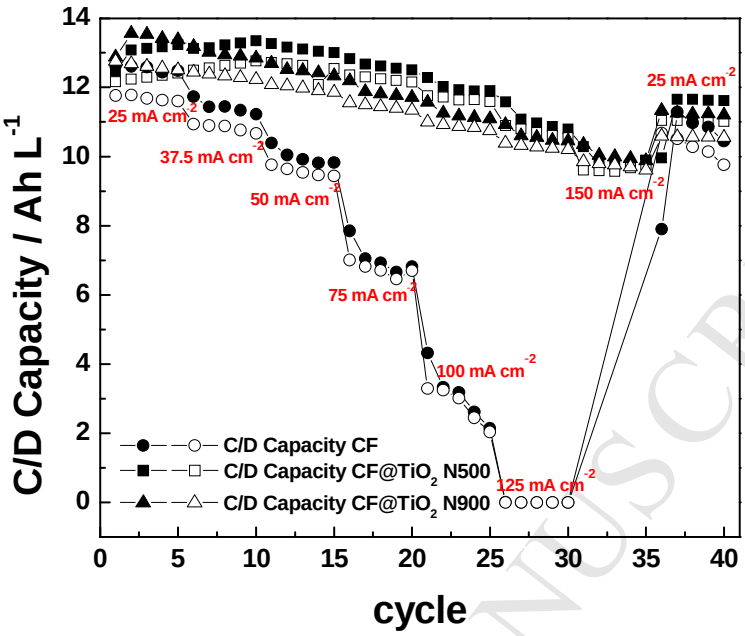

Figure S9. Battery's capacity as a function of the current density for different modified electrode used as, CF-HT, CF@TiO_2 N500 and CF@TiO_2 N900.

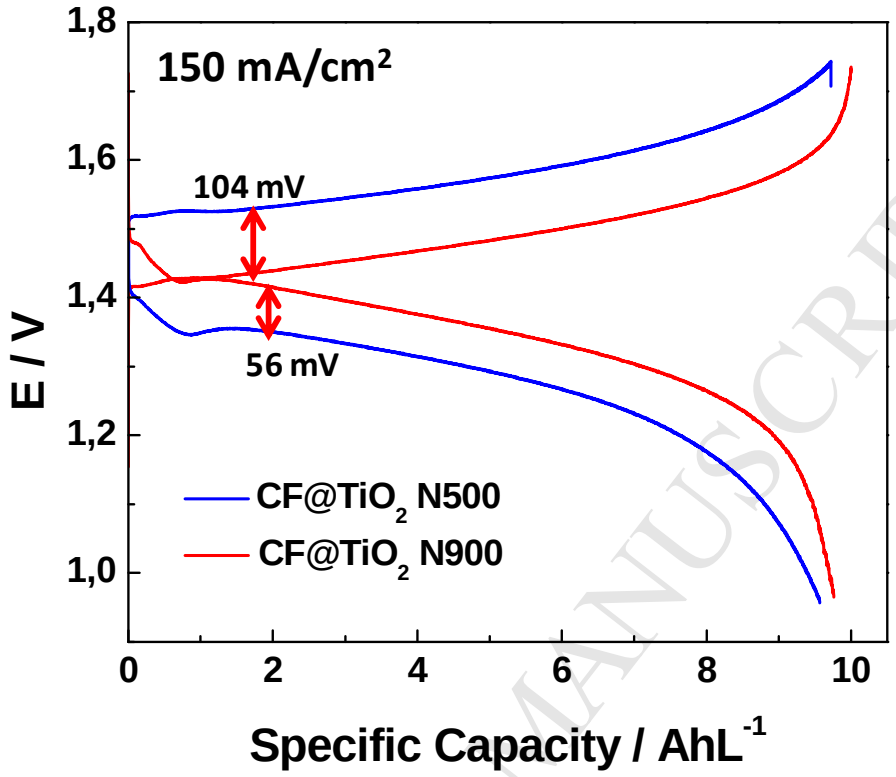

Figure S10 – Comparative between voltage profiles for CF@TiO_2 N500 and CF@TiO_2 N900 for current density applied of 150 *mA* cm^{-2}.

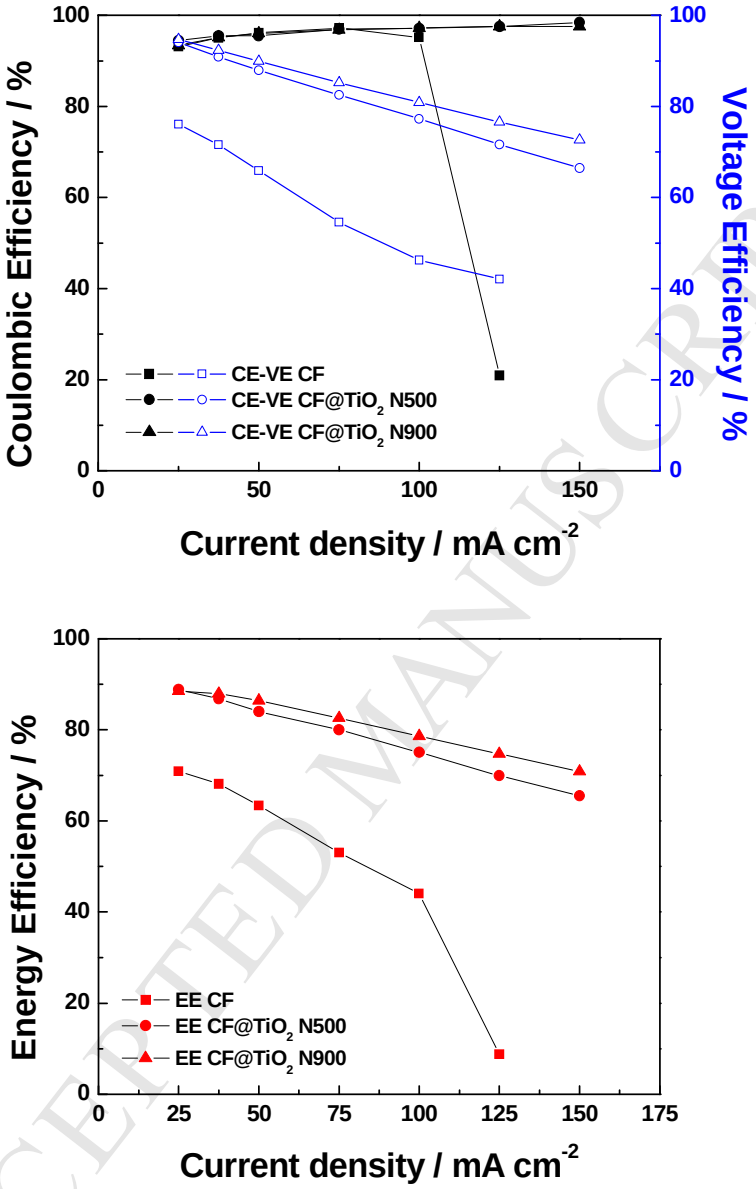

Figure S11. Average efficiencies (CE, VE and EE) as a function of the current density applied for different electrodes in galvanostatic single cell conditions.

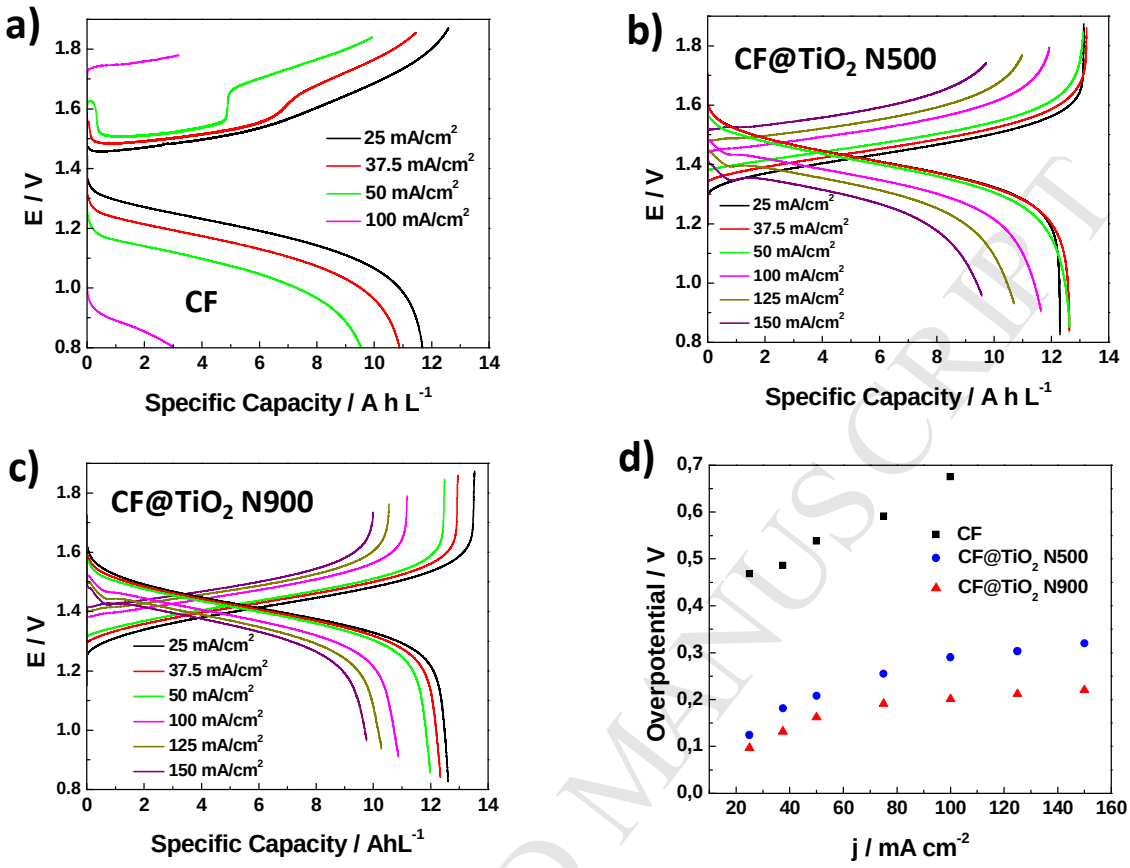

Figure S12 – Charge-discharge voltage profiles between 1.8 and 0.8 *V* at different current densities (25 to 150 *mA* cm^{-2}) for **a)** CF, **b)** CF@TiO_2 N500 and **c)** CF@TiO_2 N900. **d)** Overvoltage during charge period comparatively to E_{ocv}

Table S1. –. Electrochemical performance for single cell comparative using different treated electrodes based on physical and chemical modifications on carbonaceous structures.

Modification or activation method	Parameters of VRFB single cell								Ref
	Electrode size /cm	[$VOSO_4$] / M	Max j / mA cm^{-2}	CE / %	VE / %	EE / %	Electrolyte Utilization ratio	Cyclesmax.	
N-doped carbon	2.5 x 2.5	2	150	98.0	70.0	68.6	37.3	80 (50mA/cm^2)	[65]
CNF/CNT	2.5 x 2.5	2	100	97.7	67.5	66.0	29.9	15 (40mA/cm^2)	[66]
Bi	5 x 5	2	150	97.2	80.3	78.1	63.8	50 (50mA/cm^2)	[67]
Mn_3O_4	/	2	40	85.4	90.2	77.0	/	20 (40mA/cm^2)	[15]
WO_3	3 x3	1.5	60	95.1	81.8	78.1	62.2	50 (30mA/cm^2)	[18]
PbO_2	3 x 4	0.5	80	99.7	78.3	78.1	82.1	30 (50mA/cm^2)	[16]
Nb_2O_5(W)	2.5 x 2.5	2	150	98.3	74.3	72.8	54.1	50 (150mA/cm^2)	[68]
ZrO_2	5 x 5	2	200	93.7	71.9	67.4	56.0	200 (100mA/cm^2)	[69]
GF@TiO_2:H	2 x 2	2	200	95.8	63.7	61.0	81.6	100 (150mA/cm^2)	[29]
Mn_3O_4 NPs/CCs	2 x 2	1	400	97	73	71	94	500 (100 mA/cm^2)	[70]
GF-Ta_2O_5 NPs	5 x 5	1.6	80	95	78	74	58	100	[71]
GF-TiC	5 x 4	1.6	100	-	62	61	<29	65 (80 mA/cm^2)	[72]
N- and –WO_3 decorated CF	1.5 x 1.5	1.8	200	96	68	67	51	-	[73]

$TiNb_2O_7$-rGO	5 x 5	1.6	160	97	74	72	70	200 (120 mA/cm^2)	[74]
CF-SnO_2 NPs	5 x 5	1.5	150	97	80	78	117*	50 (50 mA/cm^2)	[75]
GF@TiO_2 N	2 x 2	1	150	97.6	72.3	72.4	74.6	70	This work

AUTHOR INFORMATION

Corresponding Author

*E-mail: cflox@irec.cat, fjvazquez@irec.cat

Author Contributions

The manuscript was written through contributions of all authors. All authors have given approval to the final version of the manuscript.

Notes

The authors declare no competing financial interests.

ACKNOWLEDGMENT

This work was partially supported by Fundación Ramón Areces from BatLimet project. Authors from IREC thank Generalitat de Catalunya for financial support through the CERCA Program, M2E (2017SGR1246), and XaRMAE network. IREC also acknowledges additional support by the European Regional Development Funds (ERDF, FEDER), by MINECO coordinated projects MAT2014-59961 and ENE2017-85087. IREC thanks the partial support from QEERI through project NPRP9-158-1-029.

REFERENCES

[1] Aaron DS, Liu Q, Tang Z, Grim GM, Papandrew AB, Turhan A, et al. Dramatic performance gains in vanadium redox flow batteries through modified cell architecture. vol. 206. 2012. doi:10.1016/j.jpowsour.2011.12.026.

[2] Bromberger K, Kaunert J, Smolinka T. A Model for All-Vanadium Redox Flow Batteries: Introducing Electrode-Compression Effects on Voltage Losses and Hydraulics. Energy Technology 2014;2:64–76. doi:10.1002/ente.201300114.

[3] Xiong B, Zhao J, Tseng KJ, Skyllas-Kazacos M, Lim TM, Zhang Y. Thermal hydraulic behavior and efficiency analysis of an all-vanadium redox flow battery. Journal of Power Sources 2013;242:314–24. doi:10.1016/J.JPOWSOUR.2013.05.092.

[4] Leung P, Li X, León CP de, Berlouis L, Low CTJ, Walsh FC. Progress in redox flow batteries, remaining challenges and their applications in energy storage. RSC Advances 2012;2:10125–56. doi:10.1039/C2RA21342G.

[5] Darling RM, Gallagher KG, Kowalski JA, Ha S, Brushett FR. Pathways to low-cost electrochemical energy storage: a comparison of aqueous and nonaqueous flow batteries. Energy Environ Sci 2014;7:3459–77. doi:10.1039/C4EE02158D.

[6] Weber AZ, Mench MM, Meyers JP, Ross PN, Gostick JT, Liu Q. Redox flow batteries: a review. Journal of Applied Electrochemistry 2011;41:1137–64. doi:10.1007/s10800-011-0348-2.

[7] Flox C, Rubio-Garcia J, Skoumal M, Vázquez-Galván J, Ventosa E, Morante JR.

Thermally Stable Positive Electrolytes with a Superior Performance in All-Vanadium Redox Flow Batteries. ChemPlusChem 2015;80:354–8. doi:10.1002/cplu.201402336.

[8] Zhang H, Zhang H, Li X, Mai Z, Zhang J. Nanofiltration (NF) membranes: the next generation separators for all vanadium redox flow batteries (VRBs)? Energy & Environmental Science 2011;4:1676. doi:10.1039/c1ee01117k.

[9] Li Y, Zhang H, Zhang H, Cao J, Xu W, Li X. Hydrophilic porous poly(sulfone) membranes modified by UV-initiated polymerization for vanadium flow battery application. Journal of Membrane Science 2014;454:478–87. doi:10.1016/j.memsci.2013.12.015.

[10] Merle G, Ioana F, Demco D, Saakes M, Hosseiny S. Friedel–Crafts Crosslinked Highly Sulfonated Polyether Ether Ketone (SPEEK) Membranes for a Vanadium/Air Redox Flow Battery. Membranes 2013;4:1–19. doi:10.3390/membranes4010001.

[11] Semiz L, Sankir ND, Sankir M. Directly Copolymerized Disulfonated Poly (arylene ether sulfone) Membranes for Vanadium Redox Flow Batteries 2014;9:3060–7.

[12] Flox C, Fàbrega C, Andreu T, Morata A, Skoumal M, Rubio-Garcia J, et al. Highly electrocatalytic flexible nanofiber for improved vanadium-based redox flow battery cathode electrodes. RSC Advances 2013;3:12056. doi:10.1039/c3ra40463c.

[13] Huang R-H, Sun C-H, Tseng T -m., Chao W -k., Hsueh K-L, Shieu F-S. Investigation of Active Electrodes Modified with Platinum/Multiwalled Carbon Nanotube for Vanadium Redox Flow Battery. Journal of the Electrochemical Society 2012;159:A1579–86. doi:10.1149/2.003210jes.

[14] González Z, Botas C, Blanco C, Santamaría R, Granda M, Álvarez P, et al. Graphite oxide-based graphene materials as positive electrodes in vanadium redox flow batteries. Journal of Power Sources 2013;241:349–54. doi:10.1016/j.jpowsour.2013.04.115.

[15] Kim KJ, Park M-S, Kim J-H, Hwang U, Lee NJ, Jeong G, et al. Novel catalytic effects of Mn3O4 for all vanadium redox flow batteries. Chemical Communications (Cambridge, England) 2012;48:5455–7. doi:10.1039/c2cc31433a.

[16] Wu X, Xu H, Xu P, Shen Y, Lu L, Shi J, et al. PbO2-modified graphite felt as the positive electrode for an all-vanadium redox flow battery. Journal of Power Sources 2014;250:274–8. doi:10.1016/j.jpowsour.2013.11.021.

[17] Han P, Wang X, Zhang L, Wang T, Yao J, Huang C, et al. RuSe/reduced graphene oxide: an efficient electrocatalyst for VO2+/VO2+ redox couples in vanadium redox flow batteries. RSC Advances 2014;4:20379. doi:10.1039/c4ra01979b.

[18] Yao C, Zhang H, Liu T, Li X, Liu Z. Carbon paper coated with supported tungsten trioxide as novel electrode for all-vanadium flow battery. Journal of Power Sources 2012;218:455–61. doi:10.1016/j.jpowsour.2012.06.072.

[19] Caglar B, Richards J, Fischer P, Tuebke J. Conductive polymer composites and coated metals as alternative bipolar plate materials for all-vanadium redox-flow batteries 2014;5. doi:10.5185/amlett.2014.amwc.1023.

[20] Chakrabarti MH, Brandon NP, Hajimolana S a., Tariq F, Yufit V, Hashim M a., et al. Application of carbon materials in redox flow batteries. Journal of Power Sources 2014;253:150–66. doi:10.1016/j.jpowsour.2013.12.038.

[21] Parasuraman A, Lim TM, Menictas C, Skyllas-Kazacos M. Review of material research and development for vanadium redox flow battery applications. Electrochimica Acta 2013;101:27–40. doi:10.1016/j.electacta.2012.09.067.

[22] Brown LD, Neville TP, Jervis R, Mason TJ, Shearing PR, Brett DJL. The effect of felt compression on the performance and pressure drop of all-vanadium redox flow batteries. Journal of Energy Storage 2016;8:91–8. doi:10.1016/J.EST.2016.10.003.

[23] Fink H, Friedl J, Stimming U. Composition of the Electrode Determines Which Half-Cell's Rate Constant is Higher in a Vanadium Flow Battery n.d. doi:10.1021/acs.jpcc.5b12098.

[24] Kaneko H, Nozaki K, Wada Y, Aoki T, Negishi A, Kamimoto M. Vanadium redox reactions and carbon electrodes for vanadium redox flow battery. Electrochimica Acta 1991;36:1191–6. doi:10.1016/0013-4686(91)85108-J.

[25] Aaron D, Sun C-N, Bright M, Papandrew AB, Mench MM, Zawodzinski TA. In Situ Kinetics Studies in All-Vanadium Redox Flow Batteries. ECS Electrochemistry Letters 2013;2:29–31. doi:10.1149/2.001303eel.

[26] Chen F, Liu J, Chen H, Yan C. Study on Hydrogen Evolution Reaction at a Graphite Electrode in the All-Vanadium Redox Flow Battery 2012;7:3750–64.

[27] Sun C-N, Delnick FM, Baggetto L, Veith GM, Zawodzinski T a. Hydrogen evolution at the negative electrode of the all-vanadium redox flow batteries. Journal of Power Sources 2014;248:560–4. doi:10.1016/j.jpowsour.2013.09.125.

[28] Ventosa E, Skoumal M, Vázquez FJ, Flox C, Morante JR. Operando studies of all-vanadium flow batteries: Easy-to-make reference electrode based on silver–silver sulfate. Journal of Power Sources 2014;271:556–60. doi:10.1016/j.jpowsour.2014.08.029.

[29] Vázquez-Galván J, Flox C, Fàbrega C, Ventosa E, Parra A, Andreu T, et al. Hydrogen-Treated Rutile TiO_2 Shell in Graphite-Core Structure as a Negative Electrode for High-Performance Vanadium Redox Flow Batteries. ChemSusChem 2017;10:2089–98. doi:10.1002/cssc.201700017.

[30] Wei L, Zhao TS, Zeng L, Zeng YK, Jiang HR. Highly catalytic and stabilized titanium nitride nanowire array-decorated graphite felt electrodes for all vanadium redox flow batteries. Journal of Power Sources 2017;341:318–26. doi:10.1016/j.jpowsour.2016.12.016.

[31] Yang C, Wang H, Lu S, Wu C, Liu Y, Tan Q, et al. Titanium nitride as an electrocatalyst for V(II)/V(III) redox couples in all-vanadium redox flow batteries. Electrochimica Acta 2015;182:834–40. doi:10.1016/J.ELECTACTA.2015.09.155.

[32] Yang M, Cui Z, DiSalvo FJ. Mesoporous titanium nitride supported Pt nanoparticles as high performance catalysts for methanol electrooxidation. Phys Chem Chem Phys 2013;15:1088–92. doi:10.1039/C2CP44215A.

[33] Oyama ST. Introduction to the chemistry of transition metal carbides and nitrides. The Chemistry of Transition Metal Carbides and Nitrides, Dordrecht: Springer Netherlands; 1996, p. 1–27. doi:10.1007/978-94-009-1565-7_1.

[34] Wang S, Zhao X, Cochell T, Manthiram A. Nitrogen-doped carbon nanotube/graphite

felts as advanced electrode materials for vanadium redox flow batteries. Journal of Physical Chemistry Letters 2012;3:2164–7. doi:10.1021/jz3008744.

[35] Wang S, Iyyamperumal E, Roy A, Xue Y, Yu D, Dai L. Vertically Aligned BCN Nanotubes as Efficient Metal-Free Electrocatalysts for the Oxygen Reduction Reaction: A Synergetic Effect by Co-Doping with Boron and Nitrogen. Angewandte Chemie International Edition 2011;50:11756–60. doi:10.1002/anie.201105204.

[36] Gong K, Du F, Xia Z, Durstock M, Dai L. Nitrogen-doped carbon nanotube arrays with high electrocatalytic activity for oxygen reduction. Science (New York, NY) 2009;323:760–4. doi:10.1126/science.1168049.

[37] Rao CV, Cabrera CR, Ishikawa Y. In Search of the Active Site in Nitrogen-Doped Carbon Nanotube Electrodes for the Oxygen Reduction Reaction. The Journal of Physical Chemistry Letters 2010;1:2622–7. doi:10.1021/jz100971v.

[38] Yu D, Nagelli E, Du F, Dai L. Metal-Free Carbon Nanomaterials Become More Active than Metal Catalysts and Last Longer. The Journal of Physical Chemistry Letters 2010;1:2165–73. doi:10.1021/jz100533t.

[39] Kim KJ, Kim Y-JJ, Kim J-HH, Park M-SS. The effects of surface modification on carbon felt electrodes for use in vanadium redox flow batteries. Materials Chemistry and Physics 2011;131:547–53. doi:10.1016/j.matchemphys.2011.10.022.

[40] Kabir H, Gyan IO, Francis Cheng I. Electrochemical modification of a pyrolytic graphite sheet for improved negative electrode performance in the vanadium redox flow battery. Journal of Power Sources 2017;342:31–7. doi:10.1016/J.JPOWSOUR.2016.12.045.

[41] Liu T, Li X, Xu C, Zhang H. Activated Carbon Fiber Paper Based Electrodes with High Electrocatalytic Activity for Vanadium Flow Batteries with Improved Power Density. ACS Applied Materials & Interfaces 2017:acsami.6b14478. doi:10.1021/acsami.6b14478.

[42] Mayrhuber I, Dennison CR, Kalra V, Kumbur EC. Laser-perforated carbon paper electrodes for improved mass-transport in high power density vanadium redox flow batteries. Journal of Power Sources 2014;260:251–8. doi:10.1016/J.JPOWSOUR.2014.03.007.

[43] Perry ML, Darling RM, Zaffou R. High Power Density Redox Flow Battery Cells n.d. doi:10.1149/05307.0007ecst.

[44] Vohra MS, Selimuzzaman SM, Al□Suwaiyan MS. NH4 +□NH3 removal from simulated wastewater using UV□TiO2 photocatalysis: effect of co□pollutants and pH. Environmental Technology 2010;31:641–54. doi:10.1080/09593331003596536.

[45] Li J, Gao L, Sun J, Zhang Q, Guo J, Yan D. Synthesis of Nanocrystalline Titanium Nitride Powders by Direct Nitridation of Titanium Oxide n.d.

[46] Alexander MR, Thompson GE, Zhou X, Beamson G, Fairley N. Quantification of oxide film thickness at the surface of aluminium using XPS. Surface and Interface Analysis 2002;34:485–9. doi:10.1002/sia.1344.

[47] Lu ZH, McCaffrey JP, Brar B, Wilk GD, Wallace RM, Feldman LC, et al. SiO2 film thickness metrology by x-ray photoelectron spectroscopy. Applied Physics Letters 1997;71:2764–6. doi:10.1063/1.120438.

[48] Amano F, Nakata M, Yamamoto A, Tanaka T. Effect of Ti3+ Ions and Conduction Band Electrons on Photocatalytic and Photoelectrochemical Activity of Rutile Titania for Water Oxidation. Journal of Physical Chemistry C 2016;120:6467–74. doi:10.1021/acs.jpcc.6b01481.

[49] Henrich VE, Cox PA. The surface science of metal oxides. Cambridge University Press; 1994.

[50] Zhang Z, Goodall JBM, Morgan DJ, Brown S, Clark RJH, Knowles JC, et al. Photocatalytic activities of N-doped nano-titanias and titanium nitride. Journal of the European Ceramic Society 2009;29:2343–53. doi:10.1016/j.jeurceramsoc.2009.02.008.

[51] Martínez-Ferrero E, Sakatani Y, Boissière C, Grosso D, Fuertes A, Fraxedas J, et al. Nanostructured Titanium Oxynitride Porous Thin Films as Efficient Visible-Active Photocatalysts. Advanced Functional Materials 2007;17:3348–54. doi:10.1002/ADFM.200700396.

[52] Yan Y, Han M, Konkin A, Koppe T, Wang D, Andreu T, et al. Slightly hydrogenated TiO $_2$ with enhanced photocatalytic performance. J Mater Chem A 2014;2:12708–16. doi:10.1039/C4TA02192D.

[53] Wang G, Wang H, Ling Y, Tang Y, Yang X, Fitzmorris RC, et al. Hydrogen-Treated TiO $_2$ Nanowire Arrays for Photoelectrochemical Water Splitting. Nano Letters 2011;11:3026–33. doi:10.1021/nl201766h.

[54] Zhao J, Lin J, Wei H, Li X, Zhang W, Zhao G, et al. Surface enhanced Raman scattering substrates based on titanium nitride nanorods. Optical Materials 2015;47:219–24.

doi:10.1016/J.OPTMAT.2015.04.067.

[55] Li C, Yang W, Liu L, Sun W, Li Q. In situ growth of TiO_2 on TiN nanoparticles for non-noble-metal plasmonic photocatalysis. RSC Advances 2016;6:72659–69. doi:10.1039/C6RA15435B.

[56] Vázquez Galván J, Flox C, Fabregas C, Ventosa E, Parra A, Andreu T, et al. Hydrogen treated Rutile TiO2 shell in graphite core structure as a negative electrode for high-performance vanadium flow batteries. ChemSusChem 2017. doi:10.1002/cssc.201700017.

[57] Bard AJ, Faulkner LR, York N, @bullet C, Brisbane W, Toronto SE. ELECTROCHEMICAL METHODS Fundamentals and Applications. 1944. doi:10.1016/B978-0-12-381373-2.00056-9.

[58] Li SC, Zhang Z, Sheppard D, Kay BD, White JM, Du Y, et al. Intrinsic diffusion of hydrogen on rutile TiO2(110). Journal of the American Chemical Society 2008;130:9080–8. doi:10.1021/ja8012825.

[59] Li W, Liu J, Yan C. Multi-walled carbon nanotubes used as an electrode reaction catalyst for VO2+/VO2+ for a vanadium redox flow battery. Carbon 2011;49:3463–70. doi:10.1016/j.carbon.2011.04.045.

[60] Kim KJ, Park M-S, Kim Y-J, Kim JH, Dou SX, Skyllas-Kazacos M, et al. A technology review of electrodes and reaction mechanisms in vanadium redox flow batteries 2015;3:16913–33. doi:10.1039/C5TA02613J.

[61] Liu M, Xiang Z, Piao J, Shi J, Liang Z. Electrochemistry of vanadium redox couples on

nitrogen-doped carbon. Electrochimica Acta 2018;259:687–93. doi:10.1016/J.ELECTACTA.2017.10.183.

[62] Jin J, Fu X, Liu Q, Liu Y, Wei Z, Niu K, et al. Identifying the Active Site in Nitrogen-Doped Graphene for the VO^{2+} /VO_2^{+} Redox Reaction. ACS Nano 2013;7:4764–73. doi:10.1021/nn3046709.

[63] Kim J, Lim H, Jyoung J-Y, Lee E-S, Yi JS, Lee D. Effects of Doping Methods and Kinetic Relevance of N and O Atomic Co-Functionalization on Carbon Electrode for V(IV)/V(V) Redox Reactions in Vanadium Redox Flow Battery. Electrochimica Acta 2017;245:724–33. doi:10.1016/J.ELECTACTA.2017.06.008.

[64] Xu C, Yang X, Li X, Liu T, Zhang H. Ultrathin free-standing electrospun carbon nanofibers web as the electrode of the vanadium flow batteries. Journal of Energy Chemistry 2017;26:730–7. doi:10.1016/J.JECHEM.2017.03.005.

[65] Park M, Ryu J, Kim Y, Cho J, Hsueh KL, Shieu FS, et al. Corn protein-derived nitrogen-doped carbon materials with oxygen-rich functional groups: a highly efficient electrocatalyst for all-vanadium redox flow batteries. Energy Environ Sci 2014;7:3727–35. doi:10.1039/C4EE02123A.

[66] Park M, Jung Y, Kim J, Lee H il, Cho J. Synergistic Effect of Carbon Nanofiber/Nanotube Composite Catalyst on Carbon Felt Electrode for High-Performance All-Vanadium Redox Flow Battery. Nano Letters 2013;13:4833–9. doi:10.1021/nl402566s.

[67] Li B, Gu M, Nie Z, Shao Y, Luo Q, Wei X, et al. Bismuth nanoparticle decorating graphite felt as a high-performance electrode for an all-vanadium redox flow battery.

Nano Letters 2013;13:1330–5. doi:10.1021/nl400223v.

[68] Li B, Gu M, Nie Z, Wei X, Wang C, Sprenkle V, et al. Nanorod niobium oxide as powerful catalysts for an all vanadium redox flow battery. Nano Letters 2014;14:158–65. doi:10.1021/nl403674a.

[69] Zhou H, Shen Y, Xi J, Qiu X, Chen L. ZrO_2 -Nanoparticle-Modified Graphite Felt: Bifunctional Effects on Vanadium Flow Batteries. ACS Applied Materials & Interfaces 2016;8:15369–78. doi:10.1021/acsami.6b03761.

[70] Zeng L, Zhao TS, Wei L, Zeng YK, Zhou XL. Mn_3O_4 Nanoparticle-Decorated Carbon Cloths with Superior Catalytic Activity for the V^{II}/V^{III} Redox Reaction in Vanadium Redox Flow Batteries. Energy Technology 2018;6:1228–36. doi:10.1002/ente.201700793.

[71] Bayeh AW, Kabtamu DM, Chang Y-C, Chen G-C, Chen H-Y, Lin G-Y, et al. Ta_2O_5 -Nanoparticle-Modified Graphite Felt As a High-Performance Electrode for a Vanadium Redox Flow Battery. ACS Sustainable Chemistry & Engineering 2018;6:3019–28. doi:10.1021/acssuschemeng.7b02752.

[72] Ghimire PC, Schweiss R, Scherer GG, Wai N, Lim TM, Bhattarai A, et al. Titanium carbide-decorated graphite felt as high performance negative electrode in vanadium redox flow batteries. Journal of Materials Chemistry A 2018;6:6625–32. doi:10.1039/C8TA00464A.

[73] Hosseini MG, Mousavihashemi S, Murcia-López S, Flox C, Andreu T, Morante JR. High-power positive electrode based on synergistic effect of N- and WO3 -decorated carbon felt for vanadium redox flow batteries. Carbon 2018;136:444–53.

doi:10.1016/J.CARBON.2018.04.038.

[74] Bayeh AW, Kabtamu DM, Chang Y-C, Chen G-C, Chen H-Y, Lin G-Y, et al. Synergistic effects of a $TiNb_2O_7$ –reduced graphene oxide nanocomposite electrocatalyst for high-performance all-vanadium redox flow batteries. Journal of Materials Chemistry A 2018;6:13908–17. doi:10.1039/C8TA03408G.

[75] Mehboob S, Ali G, Shin H-J, Hwang J, Abbas S, Chung KY, et al. Enhancing the performance of all-vanadium redox flow batteries by decorating carbon felt electrodes with SnO2 nanoparticles. Applied Energy 2018;229:910–21. doi:10.1016/J.APENERGY.2018.08.047.